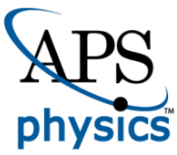

Nonlocal transport in bounded two-dimensional systems: An iterative method

J. E. Maggs and G. J. Morales

Phys. Rev. E **99**, 013307 — Published 18 January 2019

DOI: 10.1103/PhysRevE.99.013307

Nonlocal transport in bounded two-dimensional systems: an iterative method.

J. E. Maggs and G. J. Morales

Department of Physics and Astronomy
University of California, Los Angeles, California 90025 USA

Abstract

The concept of transport mediated through the dynamics of 'jumping' particles is used to develop an iterative method for obtaining steady-state solutions to the nonlocal transport equation in two dimensions (2D). The technique is self-adjoint and capable of correctly treating spatially non-uniform, asymmetric systems. An appropriate reduced version of the iteration method is used to compare with results obtained with a self-adjoint 1D transport matrix approach [Maggs and Morales, Phys. Rev. E **94,** 503302 (2016)]. The transport 'jump' probability distribution functions (*pdf*s) are based on Lévy α-stable distributions. The technique can handle the entire Lévy α-parameter range from one (Lorentz distributions) to two (Gaussian distributions). Cases with $\alpha = 2$ (standard diffusion) are used to establish the validity of the iterative method. The capabilities of the iterative method are demonstrated by presenting examples from systems with various source configurations, boundary shapes, boundary conditions and spatial variations in parameters.

I. Introduction

Nonlocal transport occurs in a variety of physical systems of limited extent, that is, systems entirely contained between confining walls or boundaries. Some examples of bounded systems exhibiting nonlocal transport in two dimensions include heat transport in semiconductor alloys [1], relaxation of photo-excited electrons in graphene [2,3], non-diffusive thermal conductivity in crystalline silicon [4], hydrodynamic electron liquids [5], hybrid topological insulators [6], heat transfer in Lennard-Jones crystals [7], two-dimensional metals [8], and heat transport in thin silicon layers and graphite sheets [9]. Also, nonlocal transport processes are observed in magnetically confined plasmas surrounded by metallic walls [10-14]. Nonlocal transport is associated with dynamical processes producing relatively large, compared to the system size, displacements or 'jumps'. Nonlocal dynamics is described by non-Gaussian probability distribution functions. A class of probability distribution functions (pdfs) inherently containing large displacements, or Lévy flights [15], is Lévy α-stable distributions. Lévy distributions contain some non-physical attributes (non-finite moments and infinite jumps) but prove useful in developing mathematical models of nonlocal transport. A key concept developed in the continuous time random walk (CTRW) [16] model is the idea of transport mediated by 'jumping' particles. The probability of information being transmitted from point (x,y) to point (x',y') depends upon a joint probability distribution function, $\eta(x-x',y-y')$. This fundamental idea is the basis of the iterative method considered in this paper.

In implementing a practical mathematical procedure to describe finite-size experiments based on Lévy α-stable *pdfs*, some difficult issues need to be overcome. They are related to the infinite extent of the jumps, as is extensively discussed in the review by Zaburdaev et al. [17], and to the interaction with the boundaries [17, 18]. One approach to handling the infinite extent of the jumps is to introduce a sharp truncation of the *pdf* at a specified cut-off [19]. Another method [20] is to introduce an exponential tempering of the spatial fractional derivatives used in a fractional Fokker-Planck equation. Vermeersch et al. [21] applied the exponential tempering directly on the Lévy *pdf* to implement a CTRW model [22-25] of thermoreflectance measurements.

The issue of a proper description of the coupling of the nonlocal system to an external world through a boundary involves the difficulties intrinsic to the infinite jumps, but there are other subtleties. An approach based on the fractional Fokker-Planck description is to postulate a 'sheath' or insulating layer whose dimension has to be judiciously chosen [26]. Another methodology, proposed by Zoia et al. [27], is to discretize the fractional Laplacian operator and solve an eigenvalue problem for free and absorbing boundaries, and in principle, to represent the solutions as a superposition of the eigenmodes. Diffusion in an open Lévy system, with a legislated reflection coefficient, has been explored by Lepri and Politi [28].

Another element for a successful modeling of a nonlocal transport experiment using Lévy *pdfs* is the capability to handle spatial variations in the parameters associated with the distributions. This situation may arise in physical systems because the internal dynamics switches character within various regions of the system, as has been found in some model comparisons [29]. Fractional diffusion in a composite medium has been addressed by Sickler and Schachinger using a finite–width boundary between layers of different fractional order [30].

For a broader perspective on the description of nonlocal transport in 2D, it should be mentioned that a significant literature exists on the subject of numerical techniques to solve 2D fractional diffusion equations. Some of these approaches include the use of alternating direction implicit methods (ADI) combined with Richardson extrapolation [31], decomposition of the coefficient matrix into a combination of sparse and structured dense matrices [32], combining the matrix transfer technique [33] with Lanczos methods [34], and a novel ADI method with Dirichlet boundary conditions [35].

The consideration of an iterative method to tackle the complexities of nonlocal transport in two-dimensions, for a bounded system whose Lévy parameters can vary with position, is a consequence of the experience obtained in prior work by the co-authors. In Ref. [36] a matrix method was introduced to describe phenomena akin to those studied in the present work, but constrained to one-dimension. A key element that emerges from that earlier effort is the necessity for the underlying methodology to preserve self-adjoint structure in systems with spatial variations in parameters. Another central concept, also arising from earlier work, is that the interface with external systems requires the implementation of intermediate boundary conditions or “fuzzy boundaries”. In extending the principles of self-adjoint structure and "fuzzy boundaries" to two-dimensional systems it is found that the iterative method is far superior to the matrix approach.

The mathematical model of jumping particle transport in 2D is presented in section II. Section III has a comparison of the iteration method, in 1D, to nonlocal self-adjoint transport-matrix results. Section IV shows 2D profiles computed with the iteration method in azimuthally symmetric cases. Section V contains a treatment of the general case and presents results from a variety of non-symmetric systems. Section VI discusses results and presents conclusions. The case of separable jumping particle *pdf*s is presented in Appendix A. Appendix B presents a method for reducing the number of iterations needed for profile convergence.

II. Mathematical model of nonlocal transport in 2D

In the study of random walks [37], the concept of 'walkers' is a fundamental tool. 'Walkers' are individual elements moving at regular time intervals from a grid point to a nearest neighbor grid point in the classical random walk process. The concept of individual 'walkers' was expanded in the continuous time random walk (CTRW) model [22] to a collection of 'particles' that wait at a grid point before

'jumping' to another grid point, not necessarily a nearest neighbor. The waiting time and the distance jumped are treated as random variables and are described by probability distribution functions (*pdf*s). The key quantities in the CTRW model are a waiting time *pdf* and a jumping distance *pdf*. The concept of jumping particles and jumping particle probability distribution functions are the main ingredients of the model used in this study to describe nonlocal transport on a discrete grid. In the present paper, motivated by heat transport experiments in plasmas [11,14], it is envisioned that the "jumping particles" carry energy packets (a scalar quantity) from a grid point in the system to other grid points in the system so that the "temperature" of the system undergoes a process of nonlocal transport. The characteristics of the jumping process are described by the jumping particle *pdf*, $P\left(\vec{x},t\right)$, where $\vec{x}$ is the vector position and t the time.

An equation determining the Fourier and Laplace transform of the *pdf* of jumping particles, $\tilde{P}\left(\vec{k},s\right)$, for a Markovian jump process (a jump process without memory) was introduced by Montroll and Weiss [22],

$$\left[1-\tilde{\psi}\left(s\right)\tilde{\eta}\left(\vec{k}\right)\right]\tilde{P}\left(\vec{k},s\right)=\frac{1-\tilde{\psi}\left(s\right)}{s}, \tag{1}$$

where $\tilde{\psi}\left(s\right)$ is the Laplace transform of the waiting time distribution. The waiting time distribution gives the probability of a particle having moved in the time interval $\left[0,\overline{t}\right],\psi\left(\overline{t}\right)d\overline{t}$. Here, a bar symbol over a spatial or temporal quantity denotes that it is measured in physical units (e.g., seconds for time and centimeters for distance). The Fourier transform of the jump *pdf* is $\tilde{\eta}\left(\vec{k}\right)$. The jump *pdf* gives the probability of a particle jumping a distance $\left|\vec{\overline{\mathbf{x}}}-\vec{\overline{\mathbf{x}}}'\right|$ from $\vec{\overline{\mathbf{x}}}'$ to $\vec{\overline{\mathbf{x}}}$. Montroll and Weiss considered an *n*-dimensional finite grid in deriving their equation. In this study, the dimensionality is taken as $n=2$. Thus the jump *pdf* is a function of the Cartesian coordinates $\left(\overline{x},\overline{x}'\right)$ and $\left(\overline{y},\overline{y}'\right)$. The waiting time probability, $\psi\left(\overline{t}\right)$, is assumed to be independent of position and the jump probability, $\eta\left(\overline{x},\overline{x}',\overline{y},\overline{y}'\right)$, is assumed to be independent of time. The initial condition is taken to be that all the particles are located at $\left(\overline{x},\overline{y}\right)=0$.

Equation (1) is simplified by assuming that the waiting time distribution is a Poisson distribution with characteristic time, $\overline{\tau}$, $\psi\left(\overline{t}\right)=\exp\left(-\overline{t}/\overline{\tau}\right)/\overline{\tau}$. The Laplace transform of the Poisson distribution is $\tilde{\psi}\left(s\right)=1/\left(1+s\overline{\tau}\right)$. With this assumption Eq. (1) becomes

$$\tilde{P}\left(\vec{k},s\right)s-1=\tilde{P}\left(\vec{k},s\right)\left(\tilde{\eta}\left(\vec{k}\right)-1\right)/\overline{\tau}. \tag{2}$$

The inverse Laplace and Fourier transforms of Eq. (2) then give an equation governing the evolution of the probability distribution in continuous space and time,

$$\frac{\partial}{\partial \bar{t}} P(\bar{x},\bar{y},\bar{t}) = \frac{1}{\bar{\tau}}\left[\int_{-\infty}^{\infty}\int_{-\infty}^{\infty} d\bar{y}'\, d\bar{x}' \left\{ \eta\left(p(\bar{x}',\bar{y}'), \bar{x}-\bar{x}', \bar{y}-\bar{y}' \right) P(\bar{x}',\bar{y}',\bar{t}) \right\} - P(\bar{x},\bar{y},\bar{t}) \right]. \quad (3)$$

The initial condition for Eq. (3) has been taken as $P(\bar{x},\bar{y},\bar{t}=0) = \delta(\bar{x})\delta(\bar{y})$, i.e., all the particles start at the origin.

The *pdf* governing the displacement of jumping particles is peaked at the point of origin of the jumpers. The origin point of the jumps uniquely identifies a set of jumping particles and thus can be used to characterize the parameters of the jump probability distribution at that point. In Eq. (3), the jumping particles are assumed to originate at the point $(\bar{x},\bar{y}) = (0,0)$ and the peak value of the *pdf* is also located at that point. The location of the peak in the jump *pdf* can be manipulated when using the Fourier transform technique and this property is used in computing the spatial form of the Lévy distributions. With the peak of the jump distribution located at $(0,0)$, the Fourier transform has the form $\tilde{\eta}\left(p(0), k_x, k_y \right)$, with $p(0)$ denoting the parameter values of the jump distribution at the point $(\bar{x},\bar{y}) = (0,0)$. In employing the jump *pdf* in transport calculations, the jump distribution peak is required to be at the spatial location $(\bar{x}',\bar{y}')$. In the process of inverting the Fourier transform, the peak of a jump distribution centered at the origin can be moved to location, $(\bar{x}',\bar{y}')$, by multiplying the Fourier transform by $\exp\left(-i\, k_x \bar{x}' - i\, k_y \bar{y}'\right)$. Also, the parameter values, $p(0)$, can be chosen to have new values, $p(\bar{x}',\bar{y}')$, that characterize the jump distribution with peak value located at $(\bar{x}',\bar{y}')$. Inverting this modified Fourier transform, $\tilde{\eta}\left(p(\bar{x}',\bar{y}'), k_x, k_y \right)\exp\left(-i\, k_x \bar{x}' - i\, k_y \bar{y}'\right)$, then gives a jump distribution with peak at $(\bar{x}',\bar{y}')$ that has the spatial form of the jump distribution in the integrand of Eq. (3), $\eta\left(p(\bar{x}',\bar{y}'), \bar{x}-\bar{x}', \bar{y}-\bar{y}' \right)$.

Solutions to equations, such as Eq. (3), are computed, in this study, on a $N \times N$ grid of evenly spaced, discrete points, $\left(\bar{x}_i, \bar{y}_j\right)$. In a discrete space, it is convenient to introduce an expression for the transported scalar quantity (like the temperature, T) in terms of individual probabilities, $T(\bar{x},\bar{y},\bar{t}) = \sum_0^{N-1}\sum_0^{N-1} A_{i,j}\, P_{i,j}(\bar{x},\bar{y},\bar{t})$, where each $P_{i,j}(\bar{x},\bar{y},\bar{t})$ satisfies Eq. (3) with the initial condition: $P_{i,j}(\bar{x},\bar{y},0) = \delta(\bar{x}-\bar{x}_i)\delta\left(\bar{y}-\bar{y}_j\right)$. The relevant equation becomes

$$\frac{\partial}{\partial \bar{t}} T(\bar{x},\bar{y},\bar{t}) = \frac{1}{\bar{\tau}} \int_{-\infty}^{\infty}\int_{-\infty}^{\infty} d\bar{y}'\, d\bar{x}' \left\{ \eta\left(p(\bar{x}',\bar{y}'), \bar{x}-\bar{x}', \bar{y}-\bar{y}'\right) T(\bar{x}',\bar{y}',\bar{t}) \right\} - \frac{1}{\bar{\tau}} T(\bar{x},\bar{y},\bar{t}) = G_S(\bar{x},\bar{y},\bar{t}) \quad , \tag{4}$$

where a source term $G_S(\bar{x},\bar{y},\bar{t})$ has been added. Physically, if *T* is identified with 'temperature', this source represents the external heating power density applied to the system.

For applications to actual experiments, it is desired to describe a system of limited physical extent, so the next assumption is that the jump distributions, η, are non-zero only over a limited spatial region, R. For convenience let the region R be square, R: $\{0 \le \bar{x} \le \bar{L},\ 0 \le \bar{y} \le \bar{L}\}$. The jump distributions are required to have zero value outside the spatial region R. The 'truncation' of the jump distributions is accomplished by multiplying them by a 'tophat' function,

$$th(\bar{x},\bar{y}) = \begin{cases} 1 & (\bar{x},\bar{y}) \in \mathrm{R} \\ 0 & (\bar{x},\bar{y}) \notin \mathrm{R} \end{cases} . \tag{5}$$

Consider the truncation of the jump distribution with peak located at the point $(\bar{x},\bar{y})$, $\eta\left(p(\bar{x},\bar{y}), \bar{x}-\bar{x}', \bar{y}-\bar{y}'\right)$. Since the jump distributions are probability densities it is required that

$$\int_{-\infty}^{\infty} d\bar{y}' \int_{-\infty}^{\infty} d\bar{x}'\ \eta\left(p(\bar{x},\bar{y}), \bar{x}-\bar{x}', \bar{y}-\bar{y}'\right) th(\bar{x}',\bar{y}') = \int_0^{\bar{L}} d\bar{y}' \int_0^{\bar{L}} d\bar{x}'\ \eta\left(p(\bar{x},\bar{y}), \bar{x}-\bar{x}', \bar{y}-\bar{y}'\right) = 1\,;\ \forall\,(\bar{x},\bar{y}) \in R \quad . \tag{6}$$

Normalizing the position variable to $\bar{L}$ and the time to $\bar{\tau}$, gives dimensionless spatial coordinates $(x,y) = (\bar{x}/\bar{L}, \bar{y}/\bar{L})$, and dimensionless time, $t = \bar{t}/\bar{\tau}$. In the new coordinates, the model transport equation for $T(x,y,t)$ is,

$$\frac{\partial}{\partial t} T(x,y,t) - \left\{ \int_0^1 dy' \int_0^1 dx'\ \eta'\left(p(x',y'), x-x', y-y'\right) T(x',y',t) - T(x,y,t) \right\} = \bar{\tau}\, G_S(x,y,t); \quad (x,y) \in R, \tag{7}$$

where $\eta' = \eta \bar{L}^2$, denotes the dimensionless jump distribution.

The primary focus of this study is the steady-state case, in which the time derivative in Eq. (7) is zero,

$$-\int_0^1 dy' \int_0^1 dx'\, \eta'\left(p(x',y'), x-x', y-y'\right) T(x',y') + T(x,y) = \overline{\tau}\, G_S(x,y) = S(x,y) \quad . \tag{8}$$

The new source (G_S multiplied by $\overline{\tau}$), $S(x,y) = \overline{\tau} G_S$, is an energy density and thus has the same units as temperature. The amplitude of the temperature is directly dependent upon the amplitude of the source, so that adjusting the source amplitude also adjusts the amplitude of the temperature. In most situations treated in this paper the maximum amplitude of the source is unity, so that the temperature can be considered as normalized to the maximum source amplitude.

The iteration method of solution is based upon the double integral term in Eq. (8). The double integral represents the processes of particles 'jumping' from all points in the system $(x',y') \in R$, and carrying the temperature at that point, $T(x',y')$ to a particular spatial location, $(x,y) \in R$. This term embodies the physical processes involved in nonlocal transport. The explicit form of the term is,

$$\int_0^1 \int_0^1 dx'\, dy' \left\{ \eta\left(p(x',y'), x-x', y-y'\right) T(x',y') \right\}. \tag{9}$$

The jump distribution in the integrand is not simply a function of, $x-x', y-y'$ because the parameters characterizing the jump distribution centered at (x',y') are allowed to vary in an arbitrary fashion as represented by the function, $p(x',y')$.

The integral operator formulation of Eq. (9) cannot, in the general case, be reduced to matrix multiplication operations. A matrix operator formulation of Eq. (9) can be obtained in the case that the 2D jump distribution can be written as the product of two, 1D jump distributions, that is, when the variables are separable. However, in the general case, the 2D jump distribution *pdf* in Eq. (9) is not separable into two 1D jump distribution *pdf*s and a technique, such as the iteration technique, that does not depend upon matrix operators is needed to find a solution. Nonetheless, it is instructive to consider the case when the 2D *pdf* is separable, and the detailed discussion of this case and its solution in terms of matrix operators is presented in Appendix A.

1). The general 'jumping' particle equation:

In the general case, in which the jump distribution function depends on 4 variables, $\eta\left(p(x',y'), x-x', y-y'\right) = \overline{\eta}(x,x',y',y)$, is not separable, and the matrix operator techniques used in the separable case discussed in Appendix A are not

available. Rather, Eq. (8) is solved using an iterative method based upon the details of the physical process embodied in Eq. (9). Before discussing the details of the iterative method it is useful to obtain a discrete form of Eq. (8) by introducing a calculation grid. The calculation grid used in this study is a collection of $N \times N$ discrete points representing the (x,y) plane. The spacing between nearest neighbor grid points is $h = 1/(N-1)$. The values of (x,y) in the calculation grid are in the space R, and thus, $0 \le x \le 1$ and $0 \le y \le 1$. Thus each point on the calculation grid is represented by a pair of indices, and $(x,y) = (ih, mh)$ with (i,m) integers and $0 \le i \le N-1$ and $0 \le m \le N-1$. The representation of spatial locations (x,y) as discrete points then implies that any function of spatial location also has a discrete representation, $T(x,y) = T(ih,mh) = T(i,m)$. In using Eq. (8), there are actually two calculation grids involved, one for the integration variables (x',y') and another for the spatial variables (x,y). Therefore, a discrete representation of Eq. (8) involves a four dimensional object $\overline{\eta}(x,x',y',y) \to \overline{\eta}(i,j,k,m)$.

Eq. (8) states that each value of the scalar quantity, *T*, in the (j,k) plane, $T(j,k)$, is distributed to the point (i,m) according to the probability '*sub-distribution*' function, $\overline{\eta}(i,:,:,m)$. In the notation, $\overline{\eta}(i,:,:,m)$, the colon symbol (:) in a slot indicates the entire range of the variable associated with the slot, while a single letter indicates the variable for that slot has the indicated value. Thus the notation, $\overline{\eta}(i,:,:,m)$, indicates that x has the value *ih*, the index *j* ranges from 0 to $N-1$ (x' ranges from 0 to 1), the index *k* ranges from 0 to $N-1$ (y' ranges from 0 to 1), and y has the value *mh*. Using the notation, $\overline{\eta}(x,x',y',y)$, for the jump distribution, the discrete form of Eq. (8) gives an expression for the temperature at each individual point in the (i,m) plane,

$$T(i,m) = \sum_{j=0}^{N-1} \sum_{k=0}^{N-1} h^2 \, \overline{\eta}_{SA}(i,j,k,m) T(j,k) + S(i,m). \qquad (10)$$

In Eq. (10) the jump distribution function $\overline{\eta}$ has been replaced with the function $\overline{\eta}_{SA}$. It is crucial for obtaining correct solutions, when the parameters are allowed to have spatial gradients, that the self-adjoint form of the jump distribution, $\overline{\eta}_{SA}$, is used. The self-adjoint form is obtained from $\overline{\eta}$ by ensuring that $\overline{\eta}_{SA}$ remains unchanged under interchange of *i* with *j* (x with x') and *k* with *m* (y with y'),

$$\overline{\eta}_{SA}(i,j,k,m) = \left[\overline{\eta}(i,j,k,m) + \overline{\eta}(j,i,m,k) \right] / 2 \, . \qquad (11)$$

Physically, the temperature at each point in the (j,k) plane, $T(j,k)$, is distributed, or spread out, by particles jumping to points in the (i,m) plane, as

represented by the term $\overline{\eta}_{SA}(:,j,k,:)$. Eq. (10) is solved using an iterative procedure. The iterative technique consists of obtaining a better estimate of the temperature profile from a previous estimate. That is, at step '*n*' in the iteration, $T_{n+1}(i,m)$ is obtained from $T_n(j,k)$ by applying Eq. (10). The first estimate of the temperature profile is not crucial, but a good guess speeds the convergence process. Two guesses for the initial profile used in this study are a constant value, $T_1 = const$ and the other is that the starting profile is the same as the source, $T_1 = S$. A technique for obtaining a good guess to the starting profile for cases when the grid size is large is presented in Appendix B. Whatever guess is chosen for the initial profile, the temperature at iteration step $n+1$is,

$$T_{n+1}(i,m) = \sum_{j=0}^{N-1}\sum_{k=0}^{N-1} h^2\, \overline{\eta}_{SA}(i,j,k,m)\, T_n(j,k) + S(i,m). \qquad (12)$$

The iterative procedure is based upon the assumption that a unique steady-state solution to Eq. (12) exists and is determined by a balance between the source input and transport to sinks, or regions of losses, generally located at the boundaries of the system. If the iterative procedure is initiated with a test profile having amplitude larger than the steady state solution, the source cannot sustain the boundary losses associated with the profile, and under iteration the profile decays (in amplitude and shape) towards the steady state solution. Similarly, an initial profile with amplitude too low, has insufficient losses at the boundaries to balance the source input. Under iteration, the profile grows in amplitude towards the steady state solution. These assertions are confirmed by subsequent computations using iteration with Eq. (12).

2). Probability distribution functions for 'jumping' particles:

In the 1D problem [36], the probability distributions representing nonlocal transport are taken from the class of Lévy α-stable distributions. A brief review of the properties of 1D Lévy α-stable distributions is appropriate before introducing the 2D form. The 1D Lévy α-stable distributions are characterized by two parameters, (α,γ), with alpha, the order of the distribution, restricted to the range, $1 \le \alpha \le 2$, and gamma, the width of the distribution, restricted to $h \le \gamma$ (*h* is the calculation grid spacing). The two parameters characterizing the distribution are allowed to be functions of position. The values $(\alpha(x),\gamma(x))$ specify the order and width of the distribution with peak at the spatial location, x. The spatial form of the 1D Lévy α-stable distribution, $L_{Levy}([\alpha(x),\gamma(x)],x-x')$ is computed numerically, using the standard fft (fast Fourier transform) algorithm, from the Lévy α-stable characteristic function [38], which has the form,

$$\ln\left(\tilde{L}_{Levy}\left([\alpha,\gamma],k_F\right)\right)=-\left(\gamma|k_F|\right)^{\alpha}. \tag{13}$$

The spatial variable, *x*, is scaled to the length of the system, $x=\overline{x}/\overline{L}$, as is the jump distribution width, $\gamma=\overline{\gamma}/\overline{L}$, where $\overline{\gamma}$ is the width measured in physical units (length). Likewise, the Fourier variable, k_F, is scaled to $\overline{L}$, $k_F=\overline{k}_F\,\overline{L}$, where $\overline{k}_F$ is measured in physical units (1/length). The notation k_F is introduced here to distinguish the Fourier wave number variable from the index variable k.

A distinctive feature of the Lévy α-stable class is that the distributions do not have finite second moments, because they decay in an algebraic fashion asymptotically. For large values of *x*, the Lévy α-stable distributions behave as, $L_{Levy}(\alpha,x)\sim 1/|x|^{1+\alpha}$, and for $\alpha<2$ this behavior leads to a non-finite second moment. The exception is the case $\alpha=2$, in which the asymptotic decay is not algebraic, but exponential, and a finite second moment exists.

The form of the 2D Lévy distribution characteristic function adopted for this study is a direct generalization of the 1D form. The procedure consists of replacing the amplitude of the 1D k-vector with the amplitude of the 2D k-vector, $|k_F|=\left(k_{F,x}^2+k_{F,y}^2\right)^{1/2}$, with $\vec{k}_F=k_{F,x}\,\hat{e}_x+k_{F,y}\,\hat{e}_y$ ($\hat{e}_x$ and $\hat{e}_y$ are unit vectors in the x and y-directions). This substitution results in distributions that are spatially isotropic about the peak location. The spatial form of the distribution is found by a 2D inverse Fourier transformation. The explicit form of the 2D Lévy characteristic function is,

$$\ln(\tilde{L}_{Levy}\left([\alpha,\gamma],|k_F|\right)=-\left(\gamma|k_F|\right)^{\alpha},\quad |k_F|=\left(k_{F,x}{}^2+k_{F,y}{}^2\right)^{1/2}. \tag{14}$$

Like the 1D Lévy distribution, the isotropic 2D distribution is characterized by two parameters, $[\alpha,\gamma]$, whose values can vary spatially with the peak location variables.

As a concrete example, the *pdf* denoted by $\overline{\eta}(:,j,k,:)$ is a 2D Lévy distribution with peak located at the spatial point corresponding to $x'=jh,\ y'=kh$. The distribution parameter set is a function of the variables (j,k), $\left[\alpha(j,k),\gamma(j,k)\right]$. The distribution with peak located at the point (j,k) is a function of the variables $(x=ih,y=mh)$. The function $\overline{\eta}(:,j,k,:)$ is computed from the characteristic function $\exp\left(-\left(\gamma(j,k)|k_F|\right)^{\alpha(j,k)}\right)$ by using the inverse fast Fourier transform in two dimensions. The inverse Fourier transform is computed on a $2N\times 2N$ grid. The positive parts of the discrete Fourier wave numbers, $k_{F,x}$ and $k_{F,y}$, range from 0 to $(N-1)2\pi$. The peak of the inverse transform, $\overline{\eta}_{2N}(:,j,k,:)$, is located at the center of

the $2N \times 2N$ grid. The peak of the inverse transform is first translated to the spatial location $(x', y') = (j, k)$ and then reduced to a $N \times N$ function of $(x, y) = (i, m)$, $\overline{\eta}(:, j, k, :)$. The function $\overline{\eta}(:, j, k, :)$ is then appropriately truncated at the boundaries and renormalized so that it satisfies the requirements of a *pdf,* namely that $\sum_{i=0}^{N-1} \sum_{m=0}^{N-1} h^2 \, \overline{\eta}(i, j, k, m) = 1$.

3). Boundaries:

The physical system is considered to consist of two spatial regions: a nonlocal transport media surrounded by a wall material. In this study, the wall material is taken as providing a perfect heat reservoir, or heat bath. That is, the wall material can maintain a uniform temperature everywhere in the boundary region. For convenience, in most cases, the uniform wall temperature is set to zero.

The probability distributions of jumping particles are terminated at the interface between the nonlocal system and the wall heat reservoir, in the sense that a particle jumping from the nonlocal system cannot jump to all locations within the wall. Particles jumping from the nonlocal system into the heat reservoir, jump to points in the wall material immediately adjacent to the nonlocal system. The distance particles jump into the wall is chosen as equal to the width of the jump distribution (measured in units of grid spacing, h) at the wall-nonlocal system interface. For example, if the jump distribution width, γ, is equal to one grid spacing ($\gamma = h$) at the wall-nonlocal system interface, then the wall region, into which particles jump, is one grid spacing wide. If the distribution width at the interface location is larger, then the overlap region is larger. For example if the distribution width at the wall is $\gamma = 3h$, then the overlap region is 3 grid points wide. This prescription creates a layer in which the material wall and the nonlocal system coexist, and provides for a smooth transition between the nonlocal system and the wall. The transition layer is the analog of the 'fuzzy' wall introduced in the previous 1D analysis of Maggs and Morales [36].

III. Comparison to 1D nonlocal transport

1). The iteration method in 1D.

Solutions to the 1D nonlocal transport problem can be found by employing a self-adjoint matrix, transport operator approach [36]. The iterative technique presented in Eq. (12) as an approach to obtain solutions to the 2D problem can also be used to obtain solutions in the 1D case. It is instructive to compare solutions obtained with these two approaches.

For the 1D problem, Eq. (12) is modified to

$$T_{n+1}(i) = \sum_{j=0}^{N-1} h\,\overline{\eta}(i,j)\,T_n(j) + S(i). \qquad (15)$$

The ith row of the variable eta-bar, $h\,\overline{\eta}(i,:)$ is a 1D *pdf* with peak value at location, $x' = j\,h$. Each row of $h\,\overline{\eta}$ represents a *pdf*, and thus the sum over each and every 'column' of $h\,\overline{\eta}$ (sum over the j-variable) is unity. Ultimately, the proper form of the $\overline{\eta}$ matrix is a self-adjoint structure with rows and columns summing to unity. To accomplish this, eta-bar undergoes the following transformations: $\overline{\eta} \rightarrow \left(\overline{\eta} + \overline{\eta}^{\dagger}\right)/2$, (with the 'dagger', †, representing the transpose operation), followed by a transformation that ensures all rows and columns sum to unity, $\overline{\eta} \rightarrow I - \left(\overline{\eta} * \boldsymbol{c1}\right) + \overline{\eta}$. In the last transformation, $\boldsymbol{I}$, is the identity matrix, and ***c1*** is a column vector with all elements equal to unity. The 'star' operator represents matrix multiplication. The final form of the transformed eta-bar satisfies the requirement that it is self-adjoint and all rows and columns sum to unity.

a. Application of the iteration method in 1D.

Figure 1 illustrates the application of Eq. (15) to obtain a solution to the simple problem with parameters values $\alpha = 2$ and $\gamma = 1$. The heat reservoir is five grid points wide on both the left and right sides, and the overlap region between the nonlocal region and the heat reservoir is one grid point wide. The temperature is set equal to zero in the heat reservoir region. The source is centrally located with a Gaussian profile, $S(x) = \exp\left(-x^2/a^2\right)$, with $a = .05$. The iteration process used to solve Eq. (15) begins with an initial temperature profile. In order to illustrate the convergence process two initial profiles are chosen. Both are spatially uniform, but one value, $T_{initial} = 100$, results in profiles that tend towards the final profile from below, while the other, $T_{initial} = 220$, gives profiles that approach the final result from above. The iteration process starts with the initial profile at step one. The value of the initial profile at all points x' is distributed to points x according to Eq. (15). The redistributed profile is then used as the starting point for step two of the iteration. The profile produced in step two of the iteration process then becomes the input for step three. The iteration process is repeated until the iterated profile converges.

A profile is considered to have converged when the logarithmic derivative of the spatially averaged value of the calculated temperature, $\overline{T}$, with respect to iteration number, is less than a chosen value. The profile convergence criteria is

$$\left|\frac{d\log\left(\overline{T}\right)}{dn_i}\right| = \left|\frac{1}{\overline{T}}\frac{d\overline{T}}{dn_i}\right| < \varepsilon. \tag{16}$$

In Eq. (16), n_i is number of iterations (a positive integer value), and $\overline{T}$ is the spatially averaged value of the profile, $\overline{T} = \sum_i \sum_m T(i,m) \big/ N^2$, always a positive quantity. The sign of the logarithmic derivative is determined by the sign of the derivative of the mean profile, $d\overline{T}/dn_i$, which of course can be negative. Since the parameter epsilon is positive, the absolute value of the logarithmic derivative is used in Eq. (16). The parameter epsilon, ε, is somewhat arbitrary, but is chosen so the change in profile with iteration number is small enough to suit the situation at hand. A typical value for epsilon is $\varepsilon = 10^{-5}$.

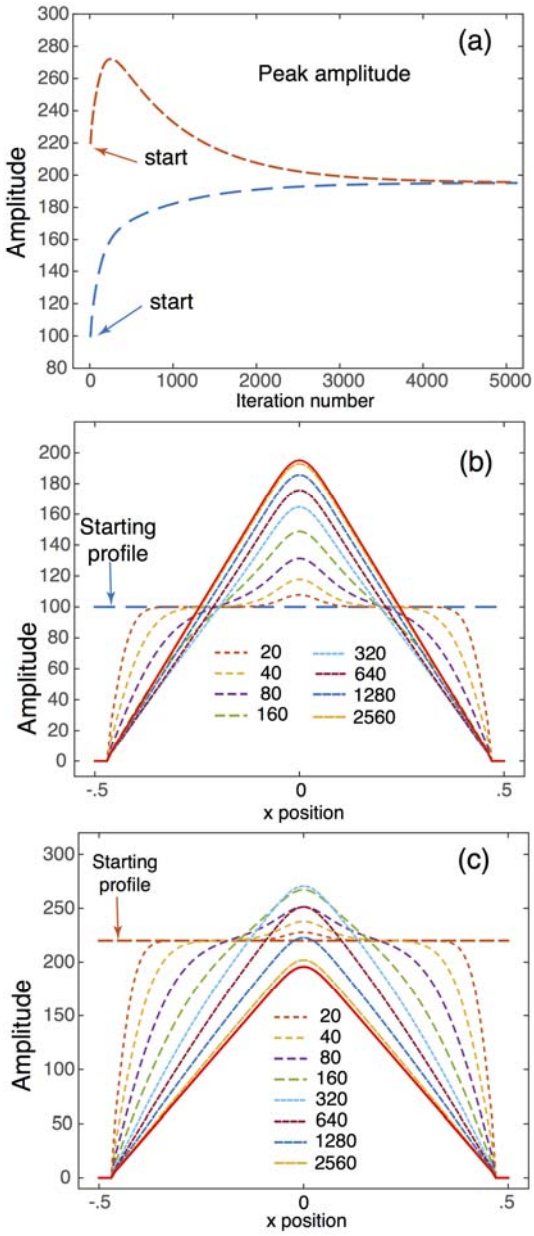

Fig. 1. Solutions to Eq. (15) are obtained by iteration. An initial profile evolves under iteration to a converged profile. (a) The behavior of the peak amplitude of the iterated profiles as the number of iterations increases for two different, uniform initial profiles. The peak value of the profile starting with uniform value 100 (dashed blue (lower) trace) steadily increases towards the converged value of the peak amplitude. The peak amplitude of the profile starting with uniform value 220 (dashed orange (upper) trace) increases at first, but then reaches a maximum value and subsequently steadily decreases towards the same value as the blue (lower) trace. (b) Profiles at various iteration steps (as noted) for the $T_{initial} = 100$ case. (c) Profiles at various iteration steps (as noted) for the $T_{initial} = 220$ case. The solid red trace in panels (b) and (c) is the converged profile ($\varepsilon = 10^{-5}$). The converged profile is the same for both starting cases.

As shown in Fig. 1a, the achievement of a converged profile requires a considerable number of iteration steps. In this example, over five thousand iterations steps are needed to obtain a converged profile. The dashed blue (lower) and dashed orange (upper) traces show the evolution of the peak profile amplitude with iteration step. The dashed blue (lower) curve is for the initial temperature profile, $T_{initial} = 100$, and the dashed orange (upper) trace is for $T_{initial} = 220$. Both initial profiles lead to the same final value for the peak amplitude. The convergent behavior displayed by the two traces was assumed, and indeed is necessary for the iteration technique to yield a steady-state profile. It is possible to develop techniques to speed up the convergence process, and a method for doing so is discussed in Appendix B.

The profiles shown in Fig. 1b and Fig. 1c illustrate the change in the iterated profile shape as the converged profile is approached. The profiles are shown at a nonlinear progression of iteration steps (1, 20, 40, 80, 160, 320, 640, 1280 and 2560) for clarity. The profiles merge as they approach the converged profile, as is made clear by comparing the difference between the profile shown at iteration step 2560 and the converged profile (solid red trace, iteration step 5120)

2). Comparison to the self-adjoint transport matrix method.

Figure 2 shows profiles obtained using the self-adjoint transport matrix method [36] compared to profiles obtained using the iteration technique. The source is the same as used in Fig. 1 and the number of grid points is, $N = 101$. Two values of the alpha parameter are considered, $\alpha = 2$ and $\alpha = 1.5$. For each value of alpha, two values of the distribution width are considered, $\gamma = 1$ and $\gamma = 3$. The boundary configuration for the iterative procedure is the fuzzy interface of the nonlocal system with the heat reservoir. The overlap region between the nonlocal system and the heat reservoir is one grid spacing in width for the $\gamma = 1$ case, and three grid spaces in width for the $\gamma = 3$ case. In the transport matrix method, the nonlocal system is bounded by material walls with high (classical) conductivity, $\kappa = 1000$. The high wall conductivity leads to uniform temperature in the wall region and thus mimics the heat reservoir boundary used in the iteration technique. The transport matrices are computed using the 'fuzzy' wall interface between the wall and nonlocal system.

In Fig. 2, profiles obtained with the transport matrix method are shown as dashed lines and the converged profiles obtained by iteration are solid lines. The case with $\gamma = 1$ is shown in Fig. 2a. The profile with $\alpha = 2$ and $\gamma = 1$, computed using the iteration technique, is the same as the converged profile in Fig. 1. The starting profile for both cases in the iteration technique was chosen to be the equal to the source. For both values of alpha, profiles obtained with the transport matrix have slightly larger peak amplitude. For $\alpha = 2$ the difference in profile amplitude is about one percent, but for $\alpha = 1.5$ it is about six percent. The insert in Fig. 2a shows

that the offset between the profiles for the $\alpha = 1.5$ case occurs at the boundary. Other than the offset at the boundary, the profile shapes are nearly identical. Figure 2b shows the profiles for the case $\gamma = 3$. It is difficult to distinguish the dashed lines from the solid lines. In this case, the two methods yield profiles that differ by less than one tenth of a percent. From the results shown in Fig. 2, it is evident that the iteration technique with a heat reservoir and fuzzy interface yields a result similar to the transport matrix with wall material of high conductivity, and a fuzzy-wall interface.

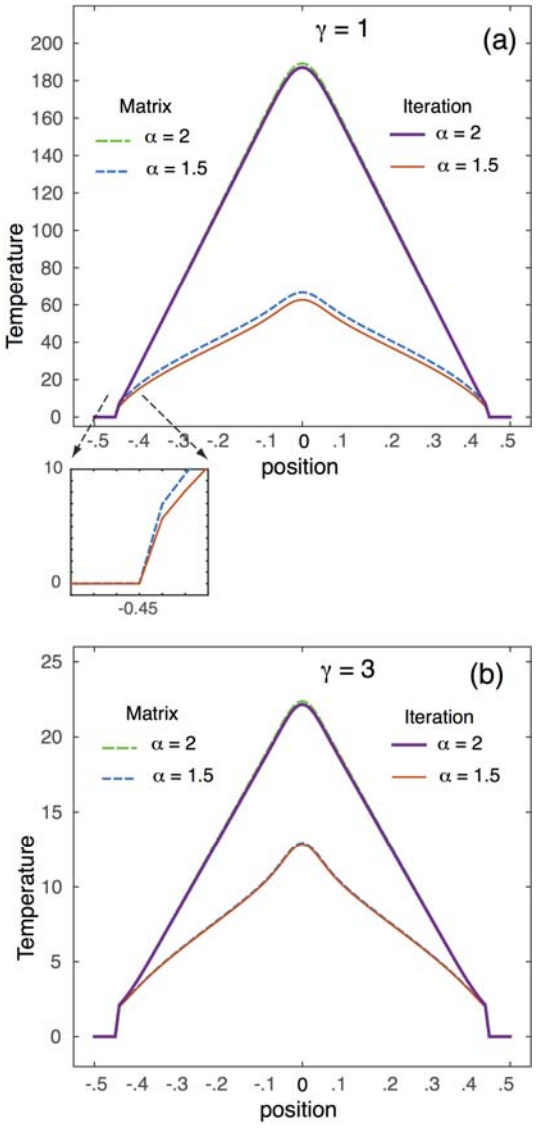

Fig. 2. A comparison of profiles obtained by iteration and profiles obtained with the transport matrix. (a) The distribution width is one grid spacing. The difference in profiles originates at the boundary. (b) The distribution width is three grid spaces. The matrix method has a material 'fuzzy' wall and the iteration technique uses a fuzzy interface with the heat reservoir.

IV. 2D profiles with Azimuthal symmetry

The simplest 2D situation is a system with azimuthal symmetry. Nonlocal transport in an azimuthally symmetric system has been investigated by Kulberg et al. [26]. In the present model, which employs a rectangular grid, an azimuthally symmetric system can be approximated by using a heat reservoir, with a circular wall, as a boundary. Since the temperature is held at a constant value of zero in the heat reservoir boundary region, the corners of the rectangular calculation grid are not relevant to the nonlocal region of the system, as is illustrated later in Figs. 3 and 4.

With a circular wall boundary, the next ingredient in an azimuthally symmetric system is an azimuthally symmetric source. Such a source is realized by requiring that the source term is a function of radial position only, $S(x,y) \to S(r)$. Finally, the parameters characterizing the 'jump' distributions must be spatially uniform, or depend only upon radial position. Figure 3 presents an example of transport in an azimuthally symmetric system with parameter values, $\alpha = 2$ and $\gamma = 1$ (gamma is measured in units of grid spacing, h). The source term is a ring, $S(r) = \exp\left((r-.15)^2/.001\right)$, and the jump distribution parameters are spatially uniform. Figure 3a shows contours of the 2D profile to demonstrate the azimuthal symmetry. The profile is computed on a 151×151 rectangular grid with a heat reservoir located at $r \geq .45$. A projection of the normalized profile along the dashed line in Fig. 3a (at $y = 0$) is shown in Fig. 3b. Also shown in Fig. 3b is a projection of the ring source along the dashed line, and the normalized 1D profile associated with the projected source. In the region interior to the ring source $(r \leq .15)$, both profiles are 'flat', but outside the ring, the 1D profile decreases linearly while the 2D profile has a 'concave' shape.

The difference between the 1D and 2D profiles is fundamental and represents the difference between the second derivative operator in one ($\frac{\partial^2}{\partial x^2}$) and two ($\frac{1}{r}\frac{\partial}{\partial r} r \frac{\partial}{\partial r}$) dimensions, as correspond to the $\alpha = 2$ case. In fact, these two operators can be inverted to obtain the 1D and 2D profiles. The 1D profile can be obtained by double integration of the source over the x-variable, $T(x) = -\int dx' \left\{ \int_0^{x'} dx\, S(x) - \frac{1}{2}\int_0^1 dx\, S(x) \right\}$. Similarly, a radial 2D profile cross-section can be obtained by double integration of the source cross-section, $T(r) = \int_0^{0.5} dr' \left\{ \int_0^{r'} dr\, rS(r) \right\} \Big/ r' - \int_0^{r} dr' \left\{ \int_0^{r'} dr\, rS(r) \right\} \Big/ r'$. To obtain the correct radial profile, the integrand of the integral over r', $\left\{ \int_0^{r'} dr\, rS(r) \right\} \Big/ r'$, must be set to zero at

$r' = 0$. In other nonlocal transport cases with $1 \le \alpha < 2$, the technique of integrating the source is not available because the transport operator is not proportional to a second derivative operator. For this reason, the case in which $\alpha = 2$ is particularly instructive.

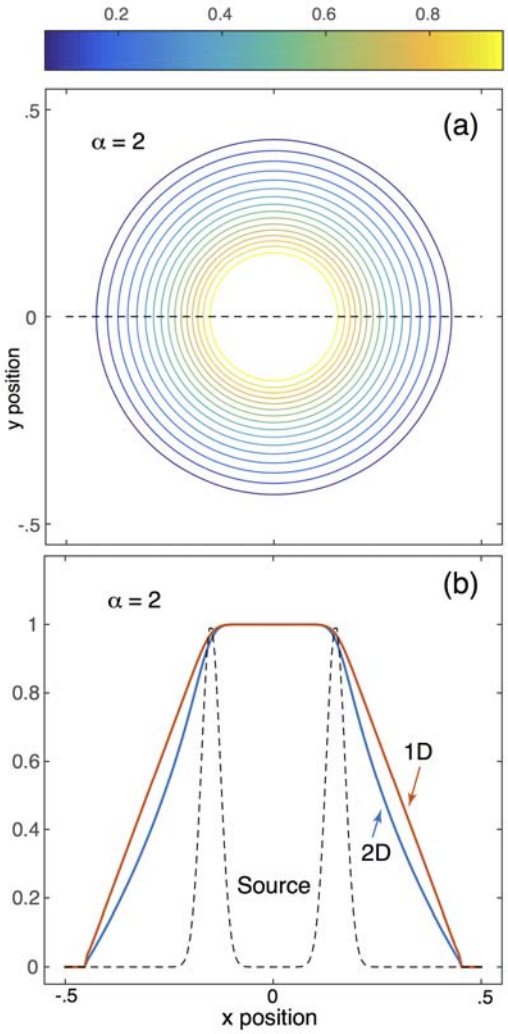

Fig. 3. (a) Contours of the 2D profile for the case $\alpha = 2$ are shown to demonstrate the azimuthal symmetry of the iteration solution. (b) A 1D profile is compared to a projection of the 2D profile along the dashed line in panel (a) (along $y = 0$). The difference in profile shape is fundamental and arises from the difference in dimensionality.

Figure 4 shows a similar situation as that shown in Fig. 3, but with nonlocal transport, $\alpha = 1.5$ and $\gamma = 1$. Figure 4a shows contours of the 2D profile and again demonstrates the azimuthal symmetry of the solution. A projection of the 2D profile along the dashed line in Fig. 4a ($y = 0$) is compared to the 1D case in Fig. 4b. This case illustrates the 'hollow' profiles that result from nonlocal transport with a 'ring' source for alpha values not equal to two. The 'concave' shape of the 2D profile

relative to the 1D profile persists. The concave profile shape is present in both cases ($\alpha = 2, 1.5$) and is, therefore, identified as a signature of the 2D geometry.

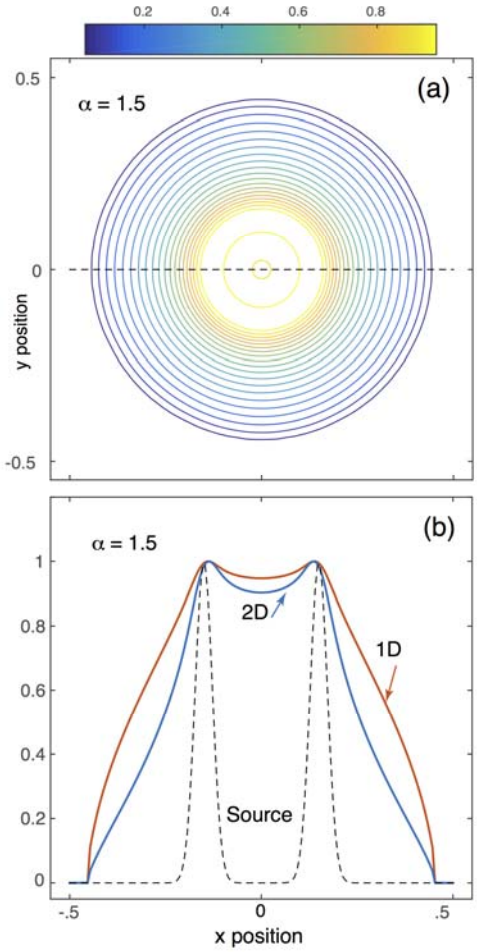

Fig. 4. (a) Contours of the 2D profile for the case $\alpha = 1.5$ are shown to demonstrate the azimuthal symmetry of the iteration solution. (b) A 1D profile is compared to a projection of the 2D profile ae dashed lilong thne in panel (a) (along $y = 0$). In the region outside the ring source, the 2D profile has a concave shape similar to the $\alpha = 2$ case (Fig. 3b), while the 1D profile now exhibits convex, rather than linear, behavior.

Nonlocal transport in the azimuthally symmetric, 2D case, with $\alpha = 1.5$, is investigated in the work by Kullberg, et al. [26]. Transport in the presence of a 'ring' source is presented in Fig. 6a of Kullberg, et al. [26]. The ring source is unity between the radial values, $.7 \le r \le .75$ and zero at radial locations outside this range. In addition to the ring source, Kullberg et al., include a constant source with amplitude $1/100$ of the ring-source maximum value. Figure 5 shows a comparison of the profile obtained using the iteration technique for similar conditions. The comparison case uses a radial coordinate with $0 \le r \le .5$ correspond to an x-coordinate ranging from $-.5 \le x \le .5$, so the comparison ring source is unity

between the values $.35 \le r \le .375$. The comparison profile has a heat reservoir boundary at $r \ge .475$, and the source does not include a constant term. The comparison profile, with the radius scaled by a factor of two is shown as the dashed 'beige' line overlying the blue 'Temperature' trace in Fig. 5. The profiles agree except near the boundary when the dashed curve goes to zero at the heat reservoir location as shown by the detailed view in Fig. 5. In the Kullberg et al. calculation, the boundary is a sheath, so a difference is expected in the boundary region. Note that agreement between the two methods is achieved by not including the small constant source in the iteration calculation.

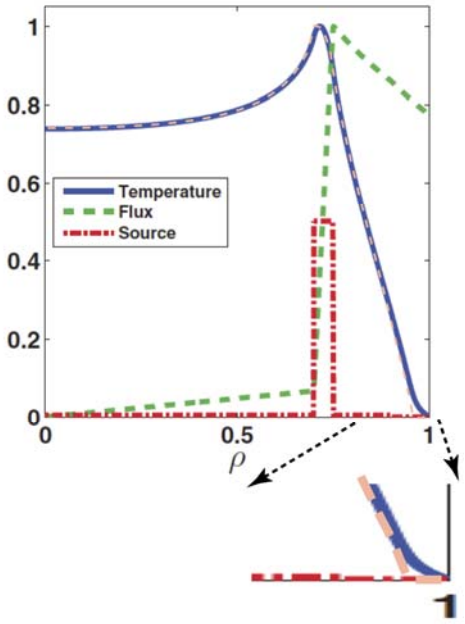

Fig. 5. A profile computed using the iteration method is compared to the profile obtained by Kullberg, et al. [26] (dashed 'beige' line overlying the blue 'Temperature' trace). The main difference in the two curves is at the boundary as seen in the expanded view.

V. The general case: 2D profiles without azimuthal symmetry

Azimuthal symmetry in a physical system can be broken by a variety of individual factors or a combination of factors. For example, variations in source configuration, boundary shape, boundary conditions and spatial variations in parameters or combinations of these factors can break symmetry. In this section several non-symmetric systems are illustrated by presenting specific examples.

a). Non-symmetric source:

Figure 6 presents a case in which the same ring source used in Figs. 3 and 4 is moved along the diagonal so that the source center is located at $(x,y)=(-.14,-.14)$. The new off-center source breaks the azimuthal symmetry. A projection of the

source shape, along the diagonal, is shown as the dashed line in Fig. 6b. The jump distribution parameters are spatially uniform. Two cases are considered: $\alpha = 2, \gamma = 1$ and $\alpha = 1.5, \gamma = 1$. The boundary condition is again a heat reservoir located at $r \geq .45$. Contours of the profile with $\alpha = 1.5$ are shown in Fig. 6a, and the

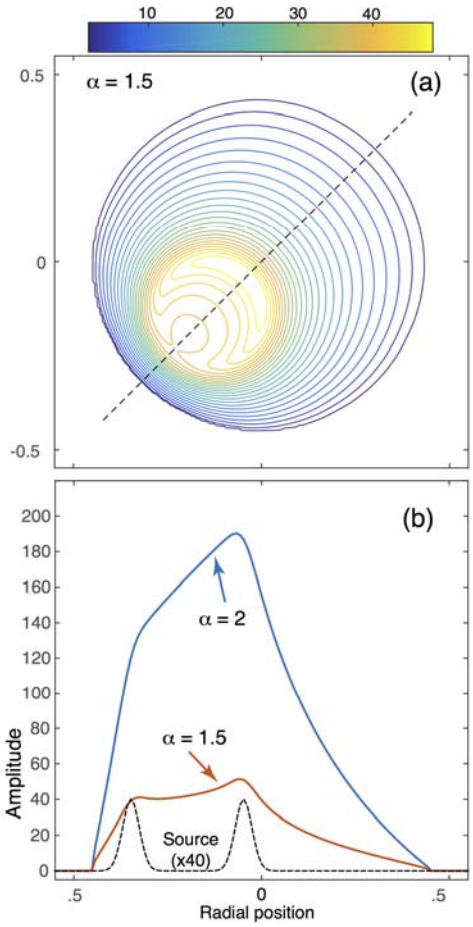

Fig. 6. (a) Contours of the solution to Eq. (8) with an off-center, ring source for the case $\alpha = 1.5, \gamma = 1$. The boundary is held at a constant temperature by a heat reservoir with a circular wall at radius $r = .45$. (b) Profile projections along the diagonal (the dashed line in (a)) for the case $\alpha = 1.5, \gamma = 1$ (solid orange line) and the case $\alpha = 2, \gamma = 1$ (solid blue line). The diagonal projection of the ring source (times forty) is shown as the dashed line.

diagonal projection (along the dashed line in Fig. 6a) is shown in Fig. 6b (orange solid line (labeled $\alpha = 1.5$)). The diagonal projection of the profile for the case with $\alpha = 2$ is also shown in Fig. 2b (blue solid line (labeled $\alpha = 2$)). The two profiles are shown without normalization in order to emphasize the difference in transport between the two alpha values. Transport is larger for the $\alpha = 1.5$ case, so the peak amplitude of the profile is smaller. The profile for the $\alpha = 2$ case is no longer flat in the center of the source region, as in Fig. 3b, and the profile for the $\alpha = 1.5$ case

retains a hollow shape, but the profile generally decreases with increasing radial value.

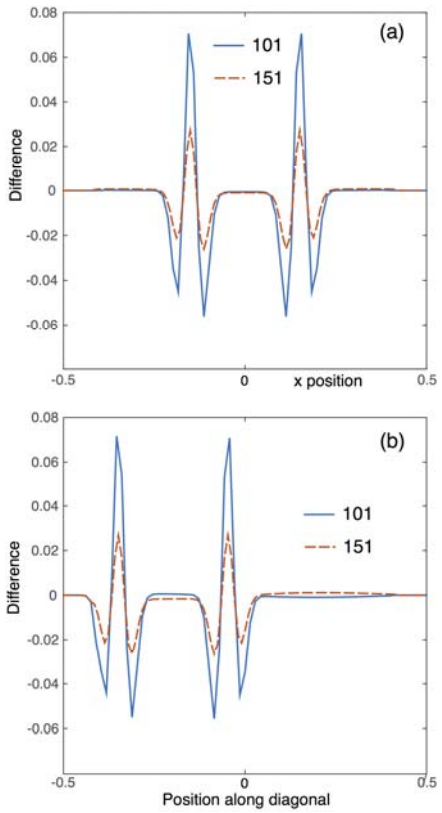

Fig. 7. Accuracy of solution to the diffusion equation ($\alpha = 2$) depends upon grid size. (a) The difference between the left- and right-hand sides of Eq. (17) along the dashed line in Fig. 3a for two calculation grid sizes as noted. (b) The difference between the left- and right-hand sides of Eq. (17) along the diagonal (dashed line) in Fig. 6a.

The validity of the profile shapes can be tested in the $\alpha = 2$ cases, the 2D profiles whose projections are shown in Fig. 3b and in Fig. 6b, because the transport operator is proportional to the second derivative operator in those cases. The profiles computed with the iteration technique can be tested as solutions to the diffusion equation, which is the governing equation for the case $\alpha = 2$. The diffusion equation in the 2D case involves the second-derivative operator in the x-direction, D_{2x}, and in the y-direction, D_{2y}. Treating the row number as the variable x, and the column number as the y variable, $D_{2x}T$ corresponds to $\partial^2 T(x,y)/\partial x^2$ and TD_{2y} corresponds to $\partial^2 T(x,y)/\partial y^2$, so that the proper 2D matrix form of the diffusion equation with uniform distribution width ($\gamma = 1$ in the present case) is,

$$\partial^2 T(x,y)/\partial x^2 + \partial^2 T(x,y)/\partial y^2 = S \quad \rightarrow \quad D_{2x}T + TD_{2y} = S. \tag{17}$$

The second derivative operators in both the x and y -directions are tri-diagonal matrices with elements $[-1,2,-1]$, with '2' being the diagonal element. Application of the two operators, as in Eq. (17), to the profiles computed by the iteration method should yield the ring source. Inserting the two $\alpha = 2$ profiles shown in Figs. 3 and 6 into the left-hand-side of Eq. (17) gives a result very close to the source term. The difference between the source term and the left-hand-side of Eq. (17) is shown in Fig. 7 for two calculation grid sizes, $N = 101$ and $N = 151$. The difference decreases with increasing grid size.

The errors arise due to the limited size of the calculation grid. The error term is proportional to the product of D_{2x} and D_{2y}, and involves a term similar to the one that arises in the separable case (see Eq. A.5 in Appendix A). For a source with scale size, L_S, the error is proportional to $(h/L_S)^2$. The error decreases with increasing grid size and vanishes in the limit $h \to 0$. The diffusion equation is recovered in this limit with $\alpha = 2$, but there is a practical upper limit to the size of the grid, and thus to the grid spacing, because of computer memory limitations. Only an approximation to the diffusion equation is achieved on a finite-sized calculation grid.

b). Non-symmetric boundary conditions:

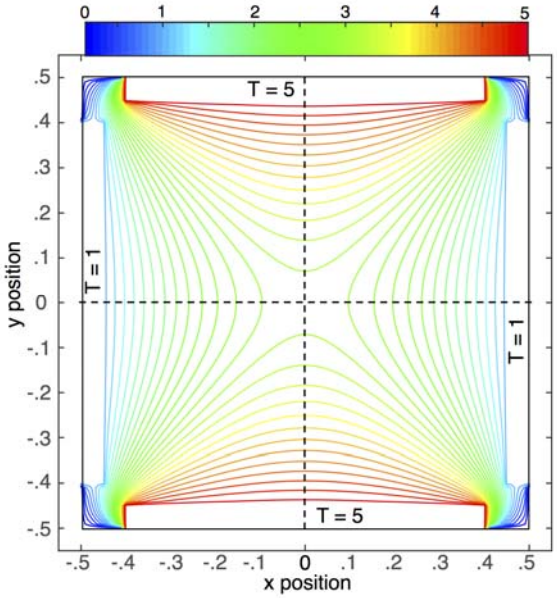

Fig. 8. Contours of constant temperature with four heat reservoirs located along the walls of the system with $\alpha = 2$. The heat reservoirs at the top and bottom keep the temperature at $T = 5$. The heat reservoirs on the left and right walls set the temperature at $T = 1$. The topology is a saddle point configuration with the saddle point at the center of the grid. Temperature profiles along the dashed lines, one in the vertical direction (constant x, x=0) and the other in the horizontal direction (constant y, y=0) are shown in Fig. 9.

Another way that azimuthal symmetry can be broken is with boundary conditions. Figure 8 shows a situation with four heat reservoirs along the boundary of the rectangular calculation grid. The values of the alpha and gamma parameters are held constant at $\alpha = 2$ and $\gamma = 1$, and there is no internal source. The reservoirs along the bottom and top walls are held at the same temperature, $T = 5$, higher than the temperature of the reservoirs along the left and right walls, $T = 1$. The boundary condition along the edges of the calculation grid outside of the reservoirs is that the temperature is zero, $T = 0$.

The topology of the four-reservoir arrangement is that of a saddle point. The saddle point is at the center of the calculation grid. The topology of the temperature contours remains the same as the value of alpha is changed. The value of the temperature at the saddle point decreases slightly as the value of alpha decreases, but the most notable change is the profile shape. Figure 9 shows a projection of the temperature profile along the vertical direction (constant x), together with a projection of the profile along the horizontal direction (constant y) for two values of alpha, $\alpha = 2$ and $\alpha = 1.2$. Transport is nonlocal for $\alpha < 2$ and thus very sensitive to boundary conditions. Transport is also stronger for smaller values of alpha. These two factors combine to give a broader profile and a lower saddle point temperature for the case with $\alpha = 1.2$.

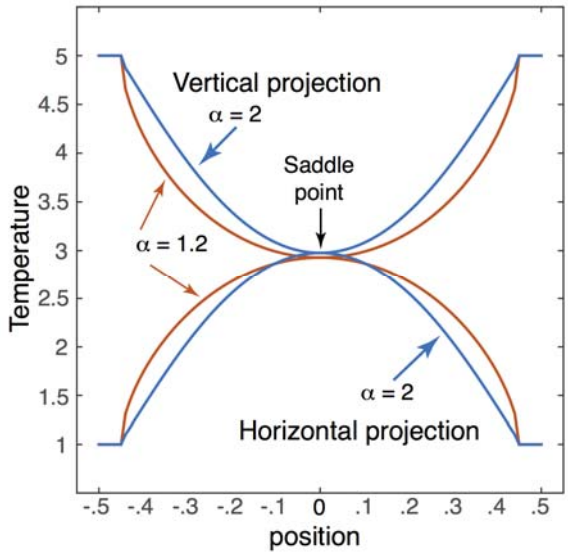

Fig. 9. Temperature profile projections for the four heat-reservoir configuration shown in Fig. 8. The 'vertical projection' is along the line dashed line at $x = 0$ shown in Fig. 8. The 'horizontal projection' is along the dashed line at $y = 0$. Profiles for two values of alpha parameter are shown, $\alpha = 2$ and $\alpha = 1.2$. The topology of the temperature contours is the same for the two values of alpha. The major difference is in the shape of the vertical and horizontal temperature profile projections, as shown.

c). Non-symmetric alpha parameter:

Situations without azimuthal symmetry can be created by choice of the spatial dependence of the jump distribution parameters. As an example of a non-symmetric system, transport in the presence of a ring of 'alpha turbulence' is explored. The geometry consists of a 'ring' source as shown in Figs. 3 and 4, but with the peak of the ring located at larger radius, $r = .4$. The 'ring' source is surrounded by a heat reservoir with $T = 0$ at radial values larger than .49 ($r \geq .49$). The ring source encloses a system in which the alpha parameter varies spatially as shown in Fig. 10. The width parameter gamma is held constant, $\gamma = 1$. The alpha parameter consists of a 'core' with $\alpha = 2$ surrounded by a ring of alpha 'turbulence' in which alpha varies both radially and azimuthally. Four different cases are considered and projections of the alpha values for each case are shown in Fig. 11. One case has constant alpha, $\alpha = 2$, and no alpha turbulence. This case sets the baseline of heating associated with classical transport. The other three cases have different mean values of alpha in the turbulent ring, $\bar{\alpha} = 1.83$, $\bar{\alpha} = 1.47$ and $\bar{\alpha} = 1.16$. Figure 10 shows contours of the values of alpha in a ring of turbulence surrounding a central core of $\alpha = 2$ for the $\bar{\alpha} = 1.83$ case. The alpha turbulence in the other two turbulent ring cases has the same spatial configuration but modified, as shown in Fig. 11, by the larger transition region to the core $\alpha = 2$ value.

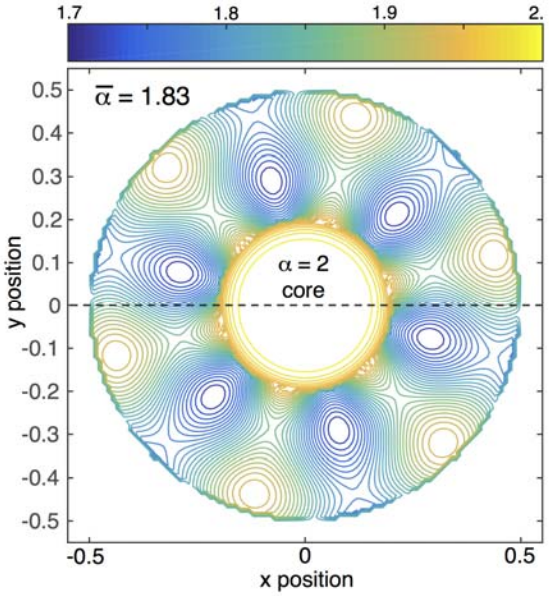

Fig. 10. Contours of alpha values for the case $\bar{\alpha} = 1.83$. This figure shows the radial and azimuthal variation of alpha values in a ring surrounding a core of alpha value two. The same turbulence pattern is used in the cases with lower mean value of alpha. Projections of alpha values along the dashed line, for the four cases, are shown in Fig. 11. The peak of the ring source is at $r = .4$.

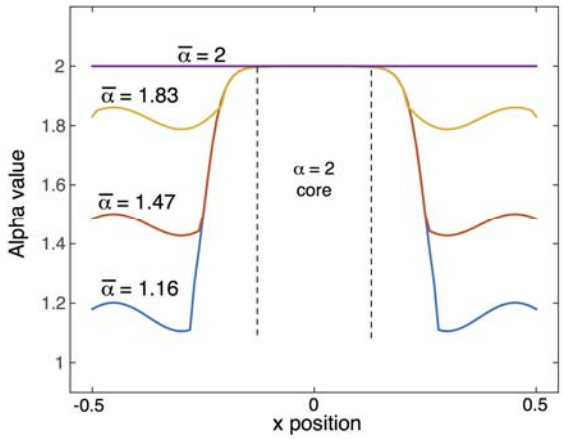

Fig. 11. Projections along the line $y = 0$ of alpha values for the four cases considered. The constant $\alpha = 2$ case sets the baseline for heating. The radial width of the alpha turbulence ring decreases for lower average values of alpha in order to accommodate the transition to the core alpha value.

Figure 12 shows the temperature profiles that result from the various spatial variations in alpha. The source is a ring with peak value located at $r = .4$ and a profile of the source (multiplied by a factor of ten) is shown for reference. The temperature for the case $\alpha = 2$ is constant inside the source. This is the expected classical behavior for constant alpha equal to two. The temperature inside the source is reduced for nonlocal transport. An average value of $\bar{\alpha} = 1.83$ reduces the temperature to about 75 percent of the value for the $\alpha = 2$ baseline case.

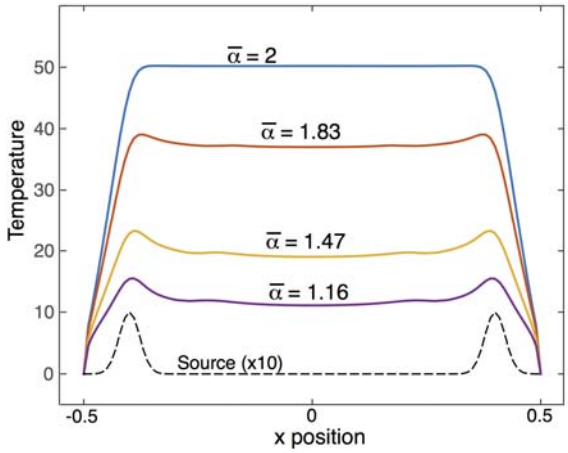

Fig. 12. Temperature profiles for the four cases of alpha variation. The central temperature decreases with decreasing value of average alpha. Heating efficiency decreases with increasing nonlocal behavior.

The profile is reduced to about 38 percent for the $\overline{\alpha} = 1.47$ case and to about 22 percent for the case with $\overline{\alpha} = 1.16$. Also, the temperature profiles increasingly display a 'hollow profile' shape, characteristic of nonlocal transport, as the average value of alpha in the 'turbulence' ring decreases.

From the examples shown, it is clear that a spatial variation in alpha value can lead to substantial reductions in the heating efficiency. Large reductions require that transport is very nonlocal, in the sense that average alpha values are closer to one than two.

d). Non-symmetric system boundary:

Another example of a non-symmetric system is one that mimics the geometry of a generic 'magnetic confinement' device. Figure 13 shows contours of 'magnetic

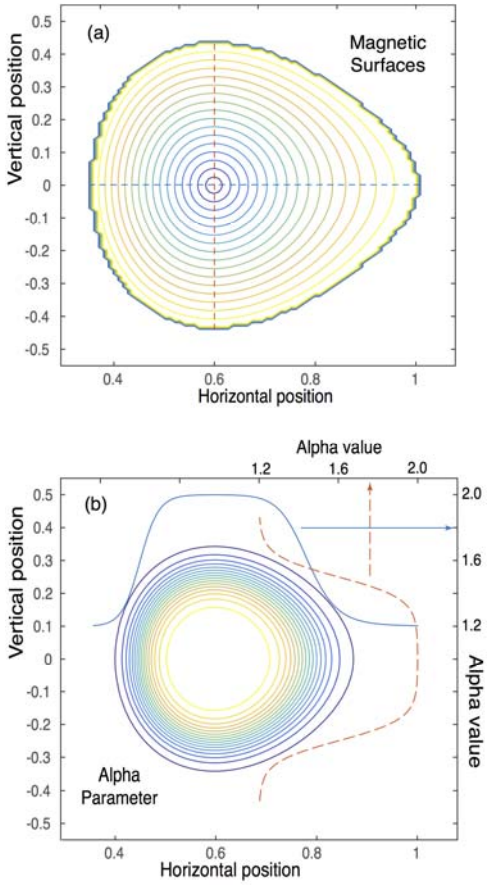

Fig. 13. (a) Magnetic surfaces in a fictional, generic confinement device. These surfaces are arbitrarily chosen for purposes of illustration. (b) Contours and cross-sections (along the dashed lines in (a)) of the spatial variation of the alpha parameter in the fictional, generic device. The spatial dependence of alpha is again arbitrarily chosen, but alpha values are constant along magnetic surfaces.

surfaces' together with the possible spatial variation of the alpha parameter in a fictional, generic confinement device. Figure 13a shows the spatial dependence of magnetic surfaces in a cross section of the fictional device. The alpha parameter values are taken to be constant along magnetic surfaces and the spatial dependence of the alpha parameter in the device is shown in Fig. 13b. The alpha parameter varies from 2 in the central region to 1.2 near the edges of the device. The spatial variation is different in the horizontal and vertical directions and there is no azimuthal symmetry in this example. The jump distribution width is chosen to be constant throughout the device, $\gamma = 1$.

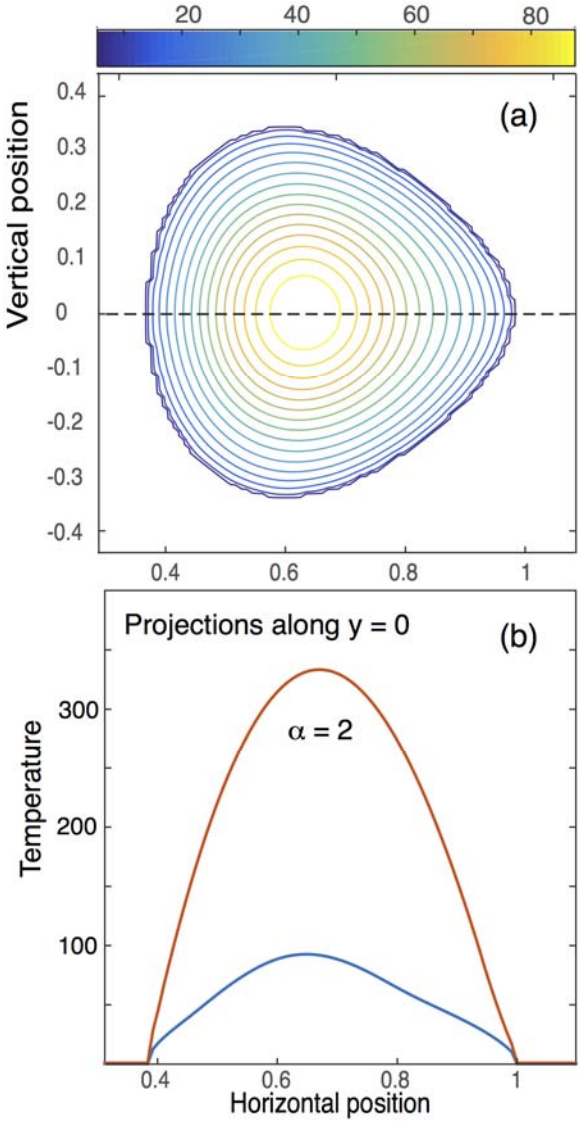

Fig. 14. (a) Contours of the temperature in the generic confinement device for a spatially constant source. The contours are not the same as the magnetic surface contours shown in Fig. 13a. (b) A profile projection at the midpoint (vertical position zero) for the non-uniform alpha case (blue (lower) trace) is compared to a profile projection from the same system, but with classical ($\alpha = 2$) transport (orange (upper) trace).

Figure 14 shows contours of the temperature profile in the fictional, generic device for a spatially constant source and with the spatial variation in alpha shown in Fig. 13. The region surrounding the device is a heat reservoir with the temperature set to zero in this region. The contours of constant temperature are similar to, but not the same as the magnetic surfaces shown in Fig. 13a. A projection of the temperature profile in the horizontal direction through the middle of the device is shown in Fig. 14b (blue (lower) trace). This profile projection is compared to a projection (orange (upper) trace) of a system with the same magnetic surfaces and constant source, but with a constant value of $\alpha = 2$ (the classical case). The profile shape is not greatly different, but transport is larger for nonlocal behavior, so that the central temperature is greatly reduced in the spatially varying alpha case.

e). Spatially varying gamma parameter:

Figure 15 shows an example of an RF (radio frequency) heating scenario in the same generic confinement device. The RF heating source is crudely modeled as a vertical rectangular region at a horizontal location outside of the central region of the device. In this example, the alpha parameter is taken to be spatially constant but the width parameter, γ, varies spatially. Gamma is smallest in the central region ($\gamma = 1$) and largest in the outer regions ($\gamma = 4$). The magenta curves (labeled as γ) in Fig. 15 show the morphology of the spatial variation in gamma and the amplitude variation in gamma is illustrated in Fig. 16 by a projection along $y = 0$. The transport coefficient (diffusion coefficient, D_c, for $\alpha = 2$) is proportional to γ^{α}, so that this particular spatial variation in gamma results in a much larger transport coefficient in the exterior regions of the device. For spatially uniform γ, transport along and across magnetic surfaces is uniform (isotropic) due to the form of the Lévy characteristic function given in Eq. (14). Spatially varying γ causes non-isotropic transport, similar to the term, $\nabla D_c \cdot \nabla T$, that appears in the case of classical diffusion for non-uniform diffusion coefficient. Figure 15 shows temperature contours associated with the RF heating source for the case $\alpha = 2$.

Two other cases are considered. One, with a spatially constant value of $\alpha = 1.5$ together with the gamma variation used in Fig. 15, and the other with a combination of the spatially varying gamma and the spatially varying alpha shown in Fig. 13. The temperature contours produced in all three cases are similar to those shown for the $\alpha = 2$ case in Fig. 15, but the profile projections differ. The profile projections for all three cases are shown in Fig. 16. The largest temperatures in the central region are achieved for the $\alpha = 2$ case. The temperature is reduced by reduced alpha values, both in the case of constant alpha ($\alpha = 1.5$) and for spatially varying alpha. In fact, the latter two cases produce nearly identical results.

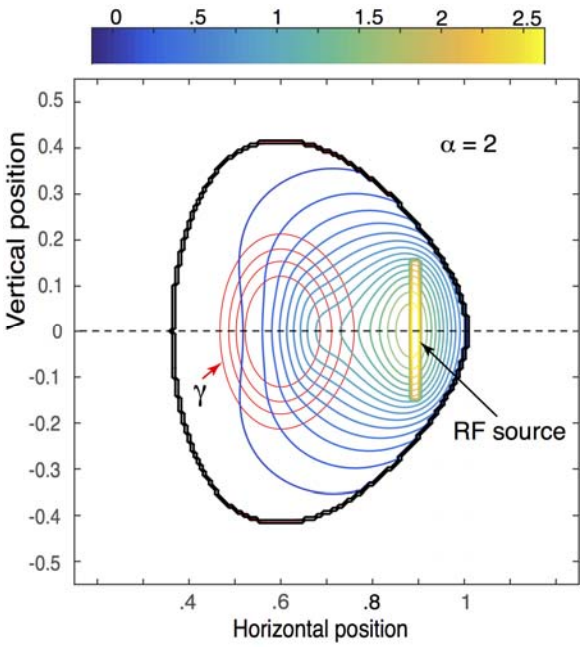

Fig. 15. An RF heating scenario in the generic confinement device. The spatial variation in gamma corresponds to spatial variation in the transport coefficient. Heating due to the RF source is concentrated by the variation in the gamma parameter, as seen from the temperature contours.

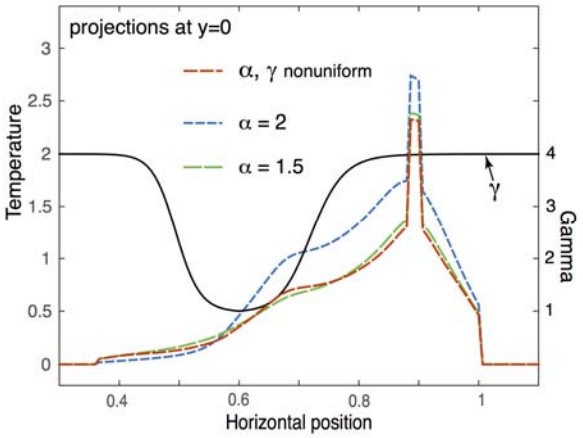

Fig. 16. Projections along $y = 0$ of the temperature profiles for three RF heating scenarios with spatially varying transport coefficient (proportional to γ^{α}). The gamma parameter varies (solid line, scale on the r.h.s.) from 1 in the center to 4 in the exterior regions. Classical transport ($\alpha = 2$) results in the largest central temperature. The case with $\alpha = 1.5$ and the spatially varying alpha case give very similar results.

These examples demonstrate the variety of physical system configurations that the iteration method can handle, including variations in source configurations, boundary shapes, boundary conditions and spatial variations in parameters.

VI. Conclusions

An iterative method for obtaining steady-state solutions to 2D nonlocal transport of scalar quantities in a bounded system is developed. The method is based upon the idea that transport is effected through, and mediated by, 'jumping' particles. Jumping particles carry information throughout the bounded system. The characteristics of the physical processes represented by the jumping particles are embodied in a 4D probability distribution function. The iterative method relies on this association. It is assumed that a unique steady-state profile exists and represents a balance between the sources and sinks in the system. This assumption is borne out in subsequent applications of the iterative method.

The capability of the 'jumping' particle technique to represent nonlocal transport relies on the type of probability distribution functions used in their description. In this study the class of Lévy α-stable distributions is used, because they clearly represent a type of nonlocal transport, namely, Levy-flights. For simplicity and clarity of presentation, the Lévy distributions used in this paper are isotropic. That is, the *pdf* at each spatial point is characterized by a single value of α and distribution width, γ. The use of isotropic distributions restricts the number of physical systems that can be represented. For example, cases with temperature anisotropies cannot be modeled with isotropic Lévy distributions. This is not a fundamental limitation, but represents an area in which the capability of the model could be extended. A practical limitation of the technique is the computer resources required. The iteration technique requires a computation involving a 4D 'stored in memory' object (the quantity $\overline{\eta}_{SA}(i,j,k,m)$, Eq. (11)) at every point on a $N \times N$ grid. Significant computer resources are required to implement the method if the grid size is large. In the examples shown, the largest grid size used in the calculations is $(151)\times(151)$. Large grid sizes are needed for accurate representation of complicated boundary shapes. In principle the grid size is not a limit on the method, but in practice it certainly is.

One of the advantages of the iteration technique, which uses the concept of jumping particles to transmit information, is that it can be expanded, in principle, to obtain solutions in *N*-dimensions. However, in practice, requirements on computer memory would limit the application of the iteration technique to no more than 3 dimensions. Another major attribute of the jumping particle method is that it is not tied to a specific computation geometry. In the examples presented, $N \times N$ calculation grids are used, but this is a matter of convenience and not necessity. The inherent geometry-independence of the iteration technique is what allows for solutions in the presence of complicated boundary configurations.

While the iteration technique was developed to solve the general 2D problem, it can be modified to handle 1D nonlocal transport. In section III results obtained with the 1D form of the iteration technique were compared to the results obtained using a transport matrix operator [36]. The comparison with 1D models also allows

for an assessment of the 2D interface between the nonlocal system and surrounding walls. In the 2D system the surrounding walls are assumed to act as heat reservoirs and hold the wall temperature at a constant value, while the 1D system uses walls with adjustable conductivity. The interface of the 2D nonlocal system with the heat reservoir has an overlap region with width the same as the jump distribution width at the interface. The comparison to 1D results shows that this overlap region is similar to the 'fuzzy wall' concept used in the 1D transport matrix method.

Examples of solutions in 2D are divided into two classes, those with azimuthal symmetry and those without. Examples of azimuthally symmetric profiles arising from a ring source are presented for two values of the alpha parameter, $\alpha = 2$ and $\alpha = 1.5$. The case with $\alpha = 2$ represents 'classical' transport (second derivative operators), while $\alpha = 1.5$ case represents a generic example of nonlocal transport. It is demonstrated that the iteration method can represent azimuthally symmetric systems even though the calculation is done on a rectangular grid. It is also shown that there is a fundamental difference in profiles computed using 1D methods and the projection of 2D profiles. The 2D profiles have an inherently 'concave' shape arising from the 2D geometry. Previous work by Kullberg et al. [26] falls in the azimuthally symmetric category, and the iteration technique was shown to reproduce the results of Kullberg et al.

Since the entire range of the alpha parameter, $1 \le \alpha \le 2$ is handled by the iteration method, it is benchmarked by considering the results of 'classical' transport cases ($\alpha = 2$) when transport is governed by the diffusion equation. It is demonstrated that, for the $\alpha = 2$ cases treated, the iteration technique results in steady-state profiles that are proper solutions to the diffusion equation, within the error limits introduced by finite calculation grid size.

Cases without azimuthal symmetry arise from several factors or combination of factors. Among these factors are: the form and location of the source term, the spatial shape of boundaries, boundary conditions with broken symmetry, and non-uniform spatial dependence of the parameters associated with the *pdfs* . Examples of specific cases without azimuthal symmetry are presented in Sec. V. Among the examples presented is the case of an asymmetric system arising from a non-central source location, a case with spatially non-uniform boundary conditions, and a case with spatially varying probability distribution parameter in a system with 'alpha turbulence'. Another example presented is a system with fundamentally asymmetric geometry similar to that found in a magnetic confinement device. Non-uniformities in both the alpha and gamma parameters are considered in several 'RF heating' scenarios in the confinement device geometry. The complex examples considered in Sec. V demonstrate the ability of the iteration technique, in conjunction with the heat reservoir boundary condition, to model actual experimental systems.

Acknowledgement

This work is performed under the auspices of the Basic Plasma Science Facility (BaPSF) at the University of California, Los Angeles (UCLA), which is supported under a DOE-NSF joint agreement.

References

1. A. M. S. Mohammed, Y. R. Koh, B. Vermeersch, H. Lu, P. G. Burke, A. C. Gossard, and A. Shakouri, Nano Lett. 15, 4269 (2015).
2. S. Winnerl, F. Gottfert, M. Mittendorff, H. Schneider, M Helm, T. Winzer, E. Malic, A. Knorr, M. Orlita, M. Potemski, M. Sprinkle, C. Berger, and W. A. de Heer, J. Phys.: Condens. Matter 25 ,054202 (2013).
3. U. Briskot, I. A. Dmitriev, and A. D. Mirlin, Phys. Rev. B 89, 075414 (2014).
4. K. T. Regner, D. P. Sellan, Z. Su, C. H. Amon, A. J. H. McGaughey, and J. A. Malen, Nature Commun. 4, 1640 (2013).
5. F. Pellegrino, I. Torre, and M. Polini, Phys. Rev. B **96**, 195401 (2017).
6. Y. Xing and Q. Sun, Phys. Rev. B **89**, 085309 (2014).
7. M. N. Ovchininnikov and G. G. Kushtanova, Results in Physics **6,** 258 (2016).
8. C. Huang, Y. D. Chong, and M. A. Cazalilla, Phys. Rev. Lett. **119**, 136804 (2017).
9. A. Sellito, D. Jou, and J. Bafaluy, Proc. Royal Soc. **A 468**, 1227 (2012).
10. K. W. Gentle, R. V. Bravenec, G. Cima, H. Gasquet, G. A. Hallock, P. E. Phillips, D. W. Ross, W. L. Rowan, A. J. Wootton, T. P. Crowley, J. Heard, A. Ouroua, P. M. Schoch, and C. Watts, Phys. Plasmas 2, 2292 (1995).
11. M. R. de Baar, M. N. A. Beurskens, G. M. D. Hogeweij, and N. J. L. Cardozo, Phys. Plasmas 6, 4645 (1999).
12. R. Jha, P. K. Kaw, D. R. Kulkarni, J. C. Parikh, and ADITYA Team, Phys. Plasmas 10, 699 (2003).
13. V. Gonchar, A. Chechkin, E. Sorokovoi, V. Chechkin, L. Grigoreva, and E. Volkov, Plasma Phys. Rep. 29, 380 (2003).
14. P. Mantica and F. Ryter, C. R. Physique 7, 634 (2006).
15. P. Barthelemy, G. Bertolotti, and D. S. Wiersma, Nature Lett. 453, 495 (2008).
16. R. Klages, G. Radons and I. M. Sokolov, '*Anomalous Transport: Foundations and Applications*', Section 4.3, John Wiely & Sons (2008) ISBN 3527622985.
17. V. Zaburdaev, S. Denisov, and J. Klaftr, Revs. Mod. Phys. 87, 483 (2015).
18. C. De Mulatier, A. Rosso, and G. Scheher, J. Stat. Mech: Th. and Exp. 10, 10006 (2013).
19. R. N. Mantegna and H. E. Stanley, Phys. Rev. Lett. 73, 2946 (1994).
20. A. Cartea and D. del-Castillo Negrete, Phys. Rev. E 76, 0411105 (2007).
21. B. Vermeersch, A. M. S. Mohammed, G. Pernot, Y. R. Koh, and A. Shakouri, Phys. Rev. B 91, 085203 (2015).
22. E. Montroll and G. H. Weiss, J. Math. Phys. 6, 167 (1965).
23. E. Montroll and Scher, J. Stat. Phys. 9, 101 (1973).
24. J. Klafter and R. Sylbey, Phys. Rev. Lett. 44, 55 (1980).
25. J. Klafter, A. Blumen, and M. F. Shlesinger, Phys. Rev. A 35, 3081 (1987).
26. A. Kullberg, D. del-Castillo Negrete, G. J. Morales, and J. E. Maggs, Phys. Rev. E 87, 052115 (2013).
27. A. Zoia, A. Rosso, and M. Kardar, Phys. Rev. E 76, 021116 (2007).
28. S. Lepri and A. Politi, Phys. Rev. E 83, 030107 (2011).
29. A. Kullberg, G. J. Morales, and J. E. Maggs, Phys. Plasmas 21, 032310 (2014).

30. B. A. Sickler and E. Schachinger, Phys. Rev. E 83, 011122 (2011).
31. C. Tadjeran and M. M. Meerschaert, J. Comp. Phys. 220, 813 (2007).
32. H. Wang and T. S. Basu, SIAM J. Sci. Comput 34, A2444 (2012).
33. M. Ilic, F. Liu, I. Turner, and V. Anh, Fract. Calc. Appl. Anal. 9, 333 (2006).
34. Q. Yang, I. Turner, F. Liu, and M. Ilic, SIAM J. Sci. Compt. 33, 1159 (2011).
35. F. Liu, S. Chen, I. Turner, K. Burrage, and V. Anh, Cent. Eur. J. Phys. 11, 1221 (2013).
36. Maggs, J. E. and G. J. Morales, Phys. Rev. E 94, 053302 (2016).
37. F. Spitzer, *Principles of Random Walk*, Second Edition, Springer-Verlag, New York, New York (1976) ISBN 0387951547. Weiss, G. H., *Aspects and Applications of the Random Walk*, North-Holland, (1994) ISBN 0444816062.
38. G. Samorodnitsky and M. Taqqu, *Stable non-Gaussian random processes: stochastic models with infinite variance*, CRC Press, (1994) ISBN 0412051710.

Appendix A: The separable case

The 2D jump distribution is separable when it can be written as the product of two, 1D jump distributions,

$$\eta\left(p(x',y'),x-x',y-y'\right)=\eta_x\left(p(x',y),x-x'\right)\eta_y\left(p(x,y'),y-y'\right). \tag{A.1}$$

The two jump distributions on the right-hand side of Eq. (A.1) can be cast in the form of matrix operators. The simplest situation occurs when the two, 1D distributions, η_x and η_y, are only dependent on two variables, $\eta_x\left(p_x(x'),x-x'\right)$ and $\eta_y\left(p_y(y'),y-y'\right)$. In this case Eq. (9) can be written as

$$\iint dx'\eta_x\left(p_x(x'),\,x-x'\right)T\left(x',y'\right)\eta_y\left(p_y(y'),y-y'\right)dy'. \tag{A.2}$$

In discrete form Eq. (A.2) becomes a matrix equation,

$$\sum_{j=0}^{N-1}\sum_{k=0}^{N-1} m^x_{i,j}T_{j,k}\,m^y_{k,m}=\boldsymbol{m}^x\boldsymbol{T}\,\boldsymbol{m}^y. \tag{A.3}$$

The matrices, $\boldsymbol{m}^x$ and $\boldsymbol{m}^y$ are 1D jump distribution matrices as described in detail in Maggs and Morales [36], and are related to the full self-adjoint transport matrices as, $\boldsymbol{m}^x=-\boldsymbol{M}^x+\boldsymbol{I}$ and $\boldsymbol{m}^y=-\boldsymbol{M}^y+\boldsymbol{I}$. The full transport equation, Eq. (8), in this simple case then becomes,

$$\boldsymbol{T}=\boldsymbol{m}^x\boldsymbol{T}\,\boldsymbol{m}^y+\boldsymbol{S}. \tag{A.4}$$

Eq. (A.4) can be put in a more familiar form,

$$-\boldsymbol{M}^x\boldsymbol{T}\,\boldsymbol{M}^y+\boldsymbol{M}^x\boldsymbol{T}+\boldsymbol{T}\,\boldsymbol{M}^y=\boldsymbol{S}. \tag{A.5}$$

If the alpha parameter has the value 2 ($\alpha=2$), then the transport matrices become second derivative operators, $\boldsymbol{M}^x=\partial^2/\partial x^2$ and $\boldsymbol{M}^y=\partial^2/\partial y^2$. Eq. (A.5) then has the familiar form of the 2D diffusion equation, with diffusion coefficient, $D=1$, if the cross term, $\boldsymbol{M}^x\boldsymbol{T}\,\boldsymbol{M}^y$, is negligible,

$$\boldsymbol{M}^x\boldsymbol{T}+\boldsymbol{T}\,\boldsymbol{M}^y=\left(\frac{\partial^2}{\partial x^2}+\frac{\partial^2}{\partial y^2}\right)T=\boldsymbol{S}. \tag{A.6}$$

The solution to Eq. (A.4) is found by employing an iterative technique,

$$\boldsymbol{T}_n = \boldsymbol{m}^x \boldsymbol{T}_{n-1} \boldsymbol{m}^y + \boldsymbol{S}; n \geq 1, \tag{A.7}$$

with $\boldsymbol{T}_0 = 0$ (i.e., $T_1 = S$). The iteration is repeated until some chosen degree of accuracy is achieved. One possibility is to require the sum total of the difference between the profiles at step *m* and *m+1* to be less than epsilon, a small number,

$$\sum_{i=0}^{N-1}\sum_{j=0}^{N-1}\left(\boldsymbol{T}_{m+1}(i,j) - \boldsymbol{T}_m(i,j)\right) \leq \varepsilon. \tag{A.8}$$

The smaller the value chosen for epsilon, the larger the number of iterations required to meet the criteria. Also, the ability to meet the criteria depends upon *N*, the size of the discrete grid chosen to represent the matrix operators. It may be necessary to choose a finer grid spacing (larger *N*) to meet the desired accuracy.

The matrices in the general separable case, $\eta_x\left(p(x',y), x-x'\right)$ and $\eta_y\left(p(x,y'), y-y'\right)$ are characterized by three indices, one for each variable: (x, x') and y for η_x and (y, y') and x for η_y. It is convenient to think of these 3D structures as a '*book*' of 2D matrices. Each matrix *book* has N pages, and each page contains a single $N \times N$ matrix. For example, each page of the matrix book corresponding to the jump distribution $\eta_y\left(p(x,y'), y-y'\right)$, represents a single value of the variable x and each page contains a 2D matrix for the variables (y,y'). Denote the matrix book corresponding to the jump distribution $\eta_x\left(p(x',y), x-x'\right)$ as $\boldsymbol{L}(m,i,j)$, and the book corresponding to $\eta_y\left(p(x,y'), y-y'\right)$as $\boldsymbol{R}(k,m,i)$. In the matrix book notation the index *i* denotes the value of the variable *x*, *j* the value of x', *k* the value of y' and *m* the value of *y*. Using matrix book notation Eq. (8) becomes

$$\boldsymbol{T}(i,m) = \sum_{j=0}^{N-1}\sum_{k=0}^{N-1} \boldsymbol{L}(m,i,j)\,\boldsymbol{T}(j,k)\,\boldsymbol{R}(k,m,i) + \boldsymbol{S}(i,m). \tag{A.9}$$

In a fashion similar to that used to solve Eq. (A.2), Eq. (A.9) can be solved using an iteration technique. The solution to Eq. (A.9), at iteration step *n* is then

$$\boldsymbol{T}_n(i,m) = \sum_{j=0}^{N-1}\sum_{k=0}^{N-1} \boldsymbol{L}(m,i,j)\,\boldsymbol{T}_{n-1}(j,k)\,\boldsymbol{R}(k,m,i) + \boldsymbol{S}(i,m); n \geq 1. \tag{A.10}$$

The major difference between the iteration technique shown in Eq. (A.10) and that shown in Eq. (A.7) is that a double sum is required to find the solution $\boldsymbol{T}_n$ at each

point (i,m) in the *x-y* plane, whereas a single double sum (two matrix multiplications) gives the solution over the entire plane in Eq. (A.7). Therefore, the computation time is much longer for Eq. (A.10) as compared to Eq. (A.7). Not surprisingly, the spatially non-uniform case requires much more computation time.

Appendix B: Reducing the number of iterations

The number of iterations required to achieve a desired level of error in the computed profile depends upon the source, the value of alpha and the size of the computation grid. Profile convergence is evaluated by monitoring the behavior, with iteration number, n_i, of the mean value of the entire profile,

$$\overline{T}(n_i) = \frac{1}{(N)^2}\sum_{i,j} T(n_i, i, j). \tag{B.1}$$

The grid size is $N \times N$ and the grid spacing is $h_N = 1/(N-1)$. The mean value of the profile is chosen because it assesses the behavior of the entire profile. In the iteration process, profiles approach, but never actually reach, their asymptotic value. The measure, used in this study, of how close a profile is to its asymptotic value is the logarithmic derivative, with respect to iteration number, of the profile mean,

$$l.d.m. \equiv \left| \left[\log\left(\overline{T}\right) \right]' \right| = \left| \, d\log(\overline{T})/dn_i \right|. \tag{B.2}$$

For a given grid size, $N \times N$, the profile can be computed in a straight-forward manner by iteration as indicated by Eq. (12). However, the iteration process requires many steps to achieve convergence, and the purpose of this Appendix is to present a technique for decreasing the number of iterations needed to obtain a desired level of convergence. The number of computations required in one iteration step is proportional to the square of the number of grid points, N^2. Because of this scaling, profile convergence is relatively rapid for small grid sizes. For example, the computation time on a 21×21 size grid as compared to a 101×101 grid is $(21/101)^2 = .0432$ times smaller. Briefly, the technique used to reduce the number of iterations is to compute a converged profile for a grid size smaller than the desired grid size, and then resize and renormalize the converged profile to the larger grid. Profile convergence is then computed on the large grid size with the re-sized, renormalized profile as the starting profile.

Successful implementation of the resized profile approach requires computation of converged profiles on several smaller sized grids so that the scaling of profile amplitude with grid size can be estimated. It is necessary to have an estimate of how the profile amplitude scales with grid size in order to obtain a useful starting profile for the large grid. As a concrete example, consider the

computation of the profile associated with a 'ring' source on a $(101)\times(101)$ grid. The value of alpha is taken to be two ($\alpha = 2$) because, for fixed grid size, this alpha value requires the largest number of iterations to achieve profile convergence. The 'ring' source used in the calculations has the same analytic dependence for all grid sizes, $S = \exp\left(-(r-.15)^2/.001\right)$.

The computation of the re-sized starting profile for the $(101)\times(101)$ grid starts by computing converged profiles on three smaller sized grids, $N = [21, 31, 41]$. The degree to which the computed profiles are asymptotic is measured by the logarithmic derivative of the profile mean as shown in Figure 17.

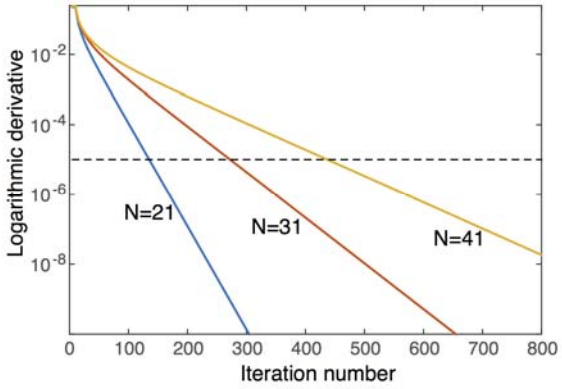

Fig. 17. The log (base 10) of the logarithmic derivative of the profile mean is shown as a function of iteration number for three 'small' grid sizes (as indicated). The dashed line indicates a value of 10^{-5}. Linearity indicates exponential decay of the logarithmic derivative.

It is important to note that the logarithmic derivative decays exponentially as the profile for a fixed grid size approaches its asymptotic value. This behavior will be exploited to obtain a 'projection' of the profile amplitude in the computation on the large grid size.

Figure 18 shows asymptotic profiles computed on three grids with $N = [21, 31, 41]$. '*Asymptotic profile*' in this instance means that $l.d.m. = \left[\log\left(\overline{T}\right)\right]' = 10^{-5}$ (see Fig. 17). The fidelity of representing the source, of course, changes with grid size and this effect is reflected in the profiles shapes. The behavior of the mean profile values on the small grids is used to extrapolate the profile mean onto the larger grid. The profile mean value, $\overline{T}$, is assumed to vary as N^a. Using the mean values of the three profiles shown in Fig. 18, the value of the parameter, a, is found to be, $a = 2.06$. The starting profile for the calculation of the large grid ($N = 101$) is obtained by using the asymptotic profile, T_{41}, obtained on the

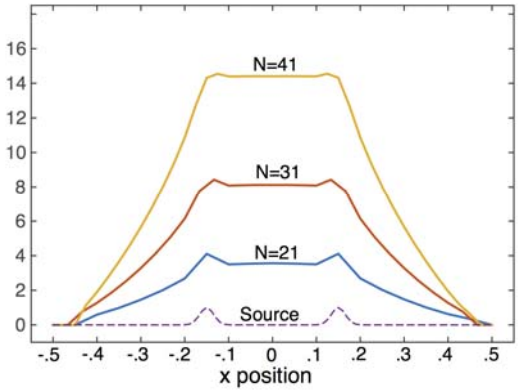

Fig. 18. The asymptotic profiles obtained for three small grids sizes. These profiles are used to obtain the amplitude scaling with grid size.

$N = 41$ grid. First the profile T_{41} is resized to a $(101)\times(101)$ grid, $T_{41} \to T_{101}^{41}$. Although most of the calculation results shown here are obtained using Matlab, the resizing is accomplished by using the IDL program '*congrid*', which is very flexible as regards grid sizes and produces excellent results with the */interp* and */minus_one* flags set. The starting profile for the calculation on the $(101)\times(101)$ grid, T_{101}^{0} is obtained by renormalizing the resized profile. Renormalization is accomplished by using the scaling parameter obtained from the behavior of the profile mean values, $T_{101}^{0} = (101/41)^{a}\, T_{101}^{41}$. The iteration process on the $(101)\times(101)$ grid is then initiated with T_{101}^{0} as the starting profile.

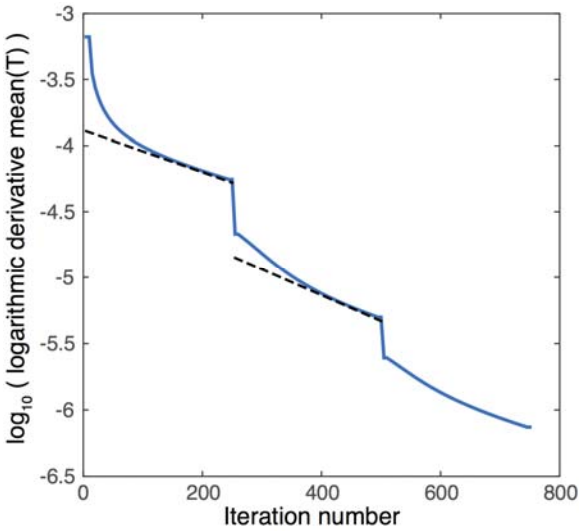

Fig. 19. The behavior of the log (base 10) of the logarithmic derivative of the profile mean value in the computation of the asymptotic profile for a ring source on a $(101)\times(101)$ grid using profile amplitude projection. The dashed lines indicate the fits used to project the profile amplitude.

Figure 19 shows the behavior of the logarithmic derivative of the profile mean value as a function of iteration number ($\log(l.d.m.)$) for the computation of the asymptotic profile on the $(101)\times(101)$ grid. The starting profile is the resized, renormalized profile obtained from the $(41)\times(41)$ grid, T_{101}^{0}. The computation consists of straight-forward iteration (Eq. 12) for 250 steps and then a 'projection' of the profile amplitude using the assumption that the logarithmic derivative of the profile mean value is decaying exponentially,

$$\frac{d}{dn_i}\log\left(\overline{T}\left(n_i\right)\right)=\exp\left(b\,n_i+c\right). \tag{B.3}$$

The constants (b,c) are obtained by fitting the log of the logarithmic derivative of the mean value, $\log\left(d\left[\log\left(\overline{T}\right)\right]/dn_i\right)$, to a straight line over the last half of the 250 step iteration range. These fits are shown in as the dashed lines in Fig. 19. Note, that the constants (b,c) are such that $\exp\left(b\,n_i+c\right)\to 0,\ n_i\to\infty$. It is found from Eq. B.3 that,

$$\log\left(\overline{T}\left(n_i\right)\right)=\exp\left(b\,n_i+c\right)/b+\log\left(\overline{T}\left(\infty\right)\right). \tag{B.4}$$

The asymptotic value of the profile mean value is 'projected' to be

$$\overline{T}\left(\infty\right)=\overline{T}\left(n_f\right)/\exp(\exp(b\,n_f+c)/b), \tag{B.5}$$

where n_f is the last of the 250 iteration steps ($n_f=250$). The final profile in the 250-step iteration process is then renormalized to have the mean value, $\overline{T}\left(\infty\right)$, and another 250 iteration steps are performed. The process is repeated until the desired accuracy is obtained. As shown in Fig. 19, the logarithmic derivative is below 10^{-6} in less than 750 iterations.

The curves shown in Fig. 17 can be used to estimate the number of iterations required to achieve a certain value of the logarithmic derivative by assuming that the number of iterations varies as N^d. For a value of *l.d.m.* (Eq. B.2) equal to 10^{-6}, the scale parameter for the required number of iterations is, $d=1.82$. The number of iterations required to have $l.d.m.=10^{-6}$ for $N=41$ is $n_i=570$. Using this information, the estimated number of iterations needed to have $l.d.m.=10^{-6}$ for $N=101$ is $n_i=570\cdot\left(101/41\right)^d=2940$. The profile projection technique can decrease calculation times considerably. The computation time need to obtain the asymptotic profiles for the $N=\left[21,31,41\right]$ cases is equivalent to about 135 iteration steps with

$N = 101$. Including this overhead, the computation time is reduced by about two-thirds, for this specific example, with the use of the profile projection technique.